3 APPLICATION OF THE ANALYTICAL SOLUTION

Figure 3.0.1) The global area for further investigations is marked in violet.

The concept of convolution with the analytical solution will be applied to the oceanic and the continental lithosphere. Thereby I will not give a complete interpretation of the calculated T_e / D distribution. This study provides a method for calculation of the elastic parameters of the lithosphere by using a new derived analytical solution. In view of this fact my intention is a verification and confirmation of the results and to give a discussion about the possible errors made in computation. Therefore only preliminary results will be presented, which provide a pre-examination and not a complete geological interpretation. This would go beyond the framework of this study and is a task for future work (Chapter 4.6).

In the following I will consider an area in South America (Figure 3.0.1). The required gravity database (SFB267/FREE UNIVERSITY OF BERLIN HTTP://WWW.FU-BERLIN.SFB267.DE) for the Andes has been collected since early 1980's. A study area in the Pacific Ocean is selected for application of the analytical solution to the oceanic lithosphere. Concerning the continental lithosphere two areas of the Andes are chosen. The location of these three areas is represented in Figure 3.0.2.

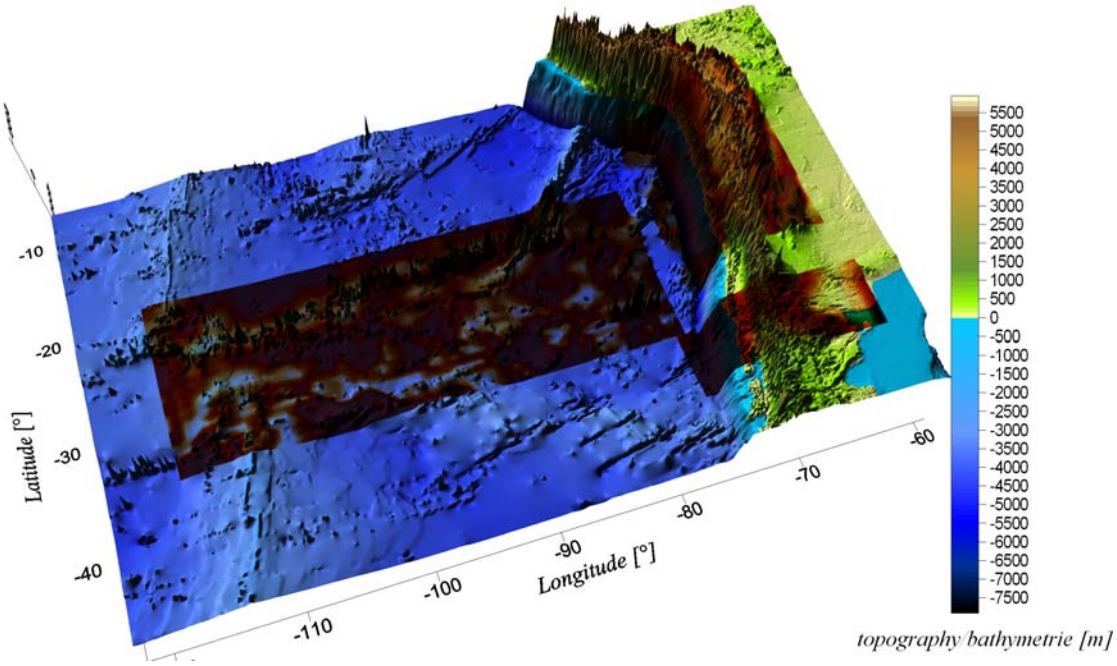

Figure 3.0.2) The three study areas are overlain over the topography.

3.1 PACIFIC OCEAN

3.1.1 Input Data

For the estimation of the elastic thickness distribution in the study area of the Pacific Ocean a database of topography, Free Air anomaly and Bouguer anomaly were used (GÖTZE ET AL. 2003).

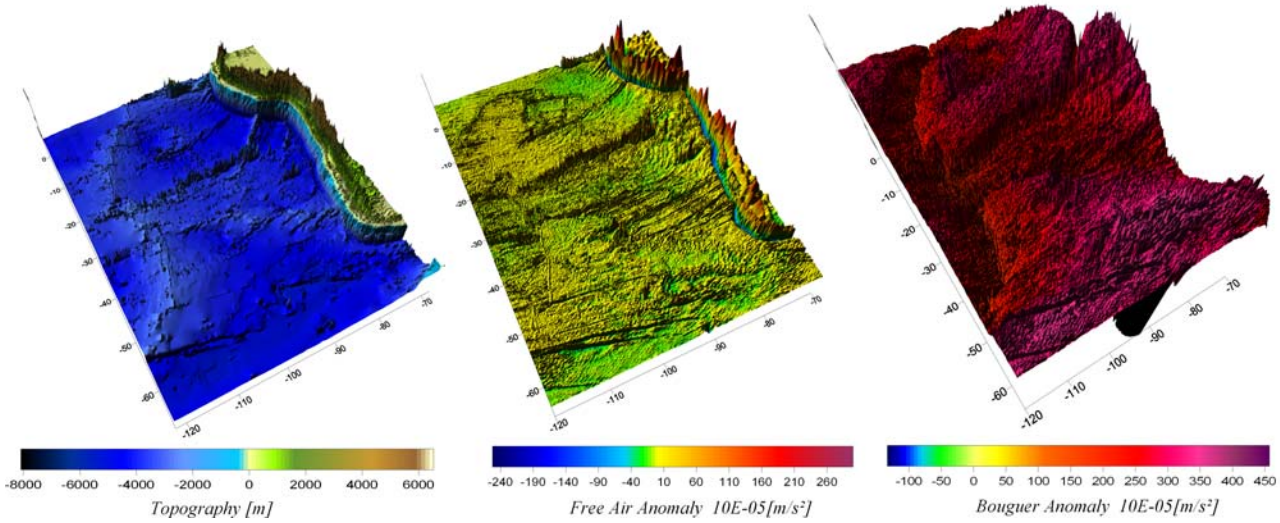

Figure 3.1.1) The topography/bathymetry, Free Air anomaly and the Bouguer anomaly data set covers the area of Pacific Ocean and have been used for the following investigations.

In Fig. 3.2.1 is the bathymetry/topography from GEBCO data shown (BRITISH OCEANOGRAPHIC DATA CENTER HTTP://WWW.BODC.AC.UK). A topographic/bathymetric correction of the Free Air anomalies (from KMS COPENHAGEN HTTP://RESEARCH.KMS.DK /GRAVITY) was calculated by Schmidt (PERS. COMM.) and provides Bouguer anomalies. The ocean water has been replaced by material with density of $2670 kg/m^3$, and the topographic masses have been removed as well.

A clear relation, who indicates a correlation coefficient $c = 1$, between the ages of the oceanic crust (obtained by MÜLLER FTP://WWW.ES.USYD.EDU.AU/PUB/AGEGRID) and the offshore Bouguer Anomaly is observed (Fig. 3.2.2). The positive Bouguer Anomalies correlate with high crustal ages. However, this trend is superimposed by numerous anomalies that are caused by different sources in the oceanic lithosphere (GÖTZE ET AL. 2003). In the following investigation a study area is chosen, where no correlation is obtained (marked with violet box, Figure 3.1.2). I aim to estimate the elastic thickness/flexural rigidity distribution within this area. Therefore the gravity crust-mantel interface (CMI) is required as reference CMI, as it was described in Chapter 2.6. Unfortunately exists no 3D density modeling in this area of investigation. In view of this fact, I will investigate first a smaller area, containing gravity observations, ship-track bathymetry and other relevant information's in order to acquire boundary conditions for the CMI depth variation.

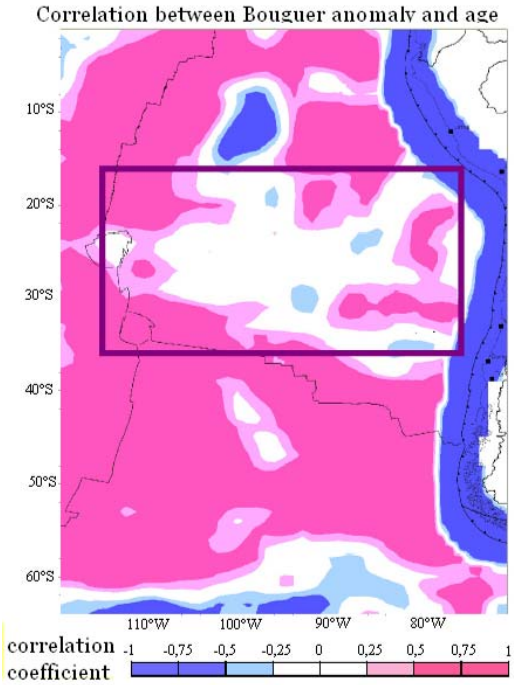

Figure 3.1.2) *shown is correlation between Bouguer anomaly and age, modification after S. Schmidt (pers. comm.). The approx. position of chosen area of investigation is marked by violet box. In this area is the correlation coefficient* $c = 0$.

3.1.2 Preliminary investigations

The smaller study area is located between $14°S - 17°S$, where two crossing wide-angle seismic refraction and reflection profiles were acquired during research vessel "Sonne" cruise (SO146-GEOPECO). HAMPEL ET AL. (2004) presented the gravity data profile coincident with the wide-angle seismic line SO146-02, for which using the software IGMAS and constraints provided by the seismic velocity model derived the density model. Beneath the ridge axis, the CMI is located $20km$ below sea level. Beneath the northwestern and southeastern ends of the profile the CMI depth values are between $16km \leq w \leq 18km$ below sea level.

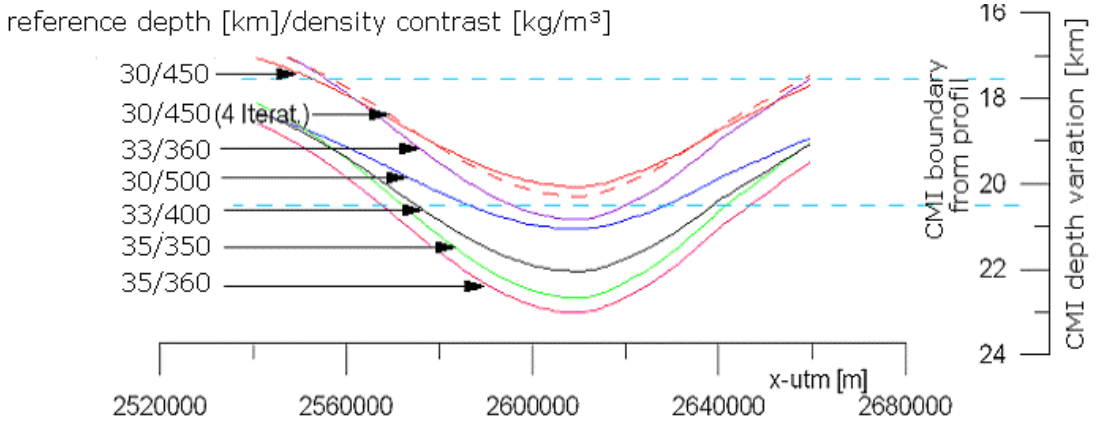

Figure 3.1.3) Different CMI were calculated for diverse density/reference depth couples. The light blue dotted line shows the maximal and minimal depth of the CMI derived by Hampel et al. (2004).

In a next step various CMI undulation were estimated by gravity inversion (see Chapter 1.3) for different density/reference depth couples (Fig. 3.1.3).
The best fit to the maximal and minimal depth of the CMI derived by HAMPEL ET. AL (2004) was obtained for the couple density contrast $\Delta\rho = 450kg/m^3$ and reference depth $30km$ and the couple density contrast $\Delta\rho = 500kg/m^3$ and reference depth $30km$. These statements about the density contrast I will use for the estimation of the elastic thickness variation in the Pacific Ocean. Since both models fit to the observation, I will use both density contrasts for further investigations.

3.1.3 Estimation of gravity CMI

Since sedimentary basins can produce a long wavelength gravity signal, they influence the correct gravity CMI estimation by gravity inversion process. Since porosity is also a function of the depth, one can use a density-porosity formula (see Appendix 5.1). The density-porosity function was insert into the "slice" program, which was introduced in Chapter 1.4. This concept was applied as well in the area of South China Sea (BRAITENBERG ET AL. 2005).

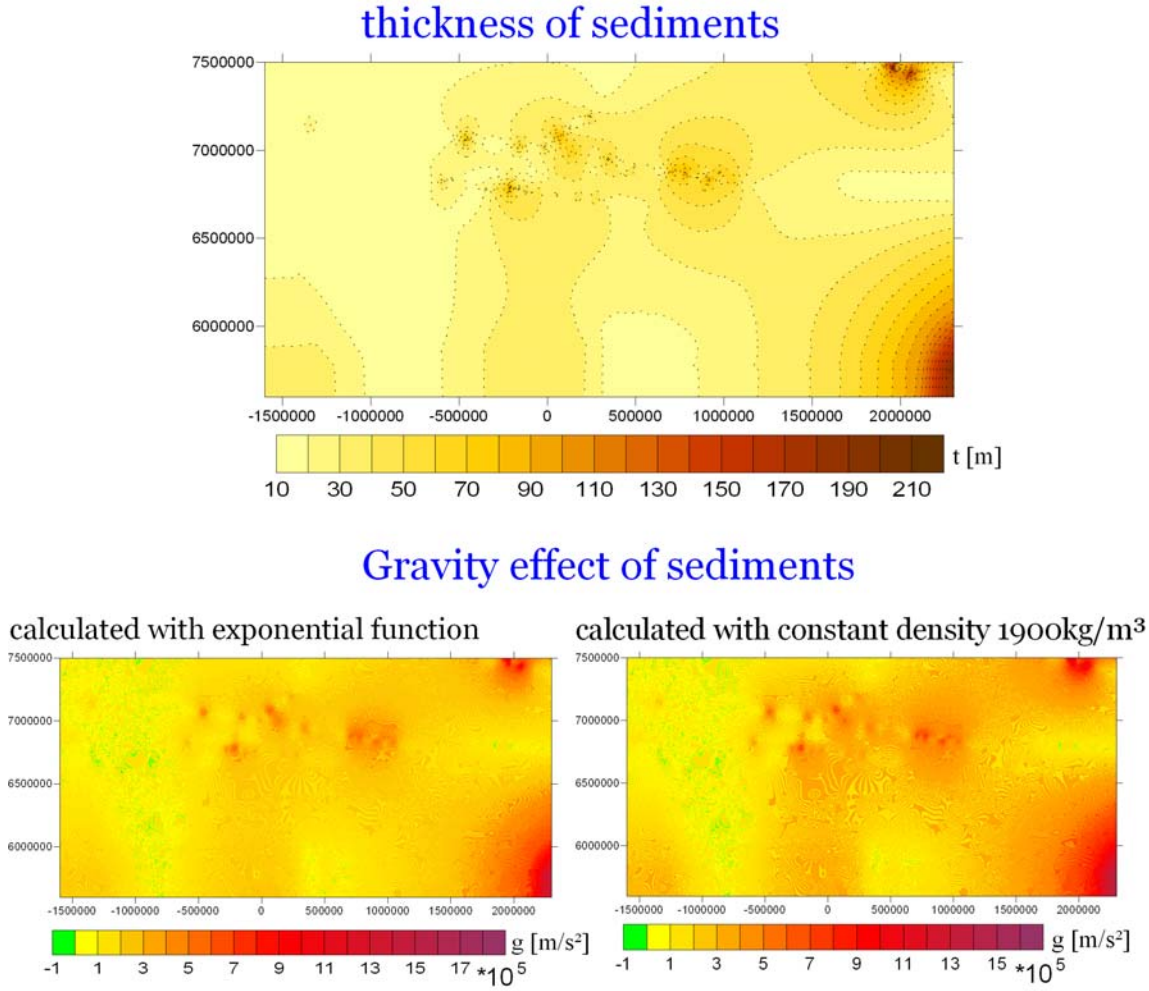

Figure 3.1.4) Shown is thickness of sediments and calculated gravity effect, computed with the depth-density function and with a constant density $\rho = 1900kg/m^3$.

After verification the slice program was used to compute the gravity effect of the sediments in the area of the Pacific Ocean, between $116-76°W$ and $37-17°S$. The sediment thickness was estimated from NOAA/NODC (NATIONAL OCEANOGRAPHIC DATA CENTER HTTP://WWW.NODC.NOAA.GOV). In the working area the thickness of sediments is very small, it varies from $t=10m$ up to $t=210m$ and increase offshore (see Fig. 3.1.4). The gravity effect g_{sed} was computed with the slice program. The density values of sediments were calculated with a density-porosity function (Appendix 5.1) and with a constant density value of $\rho_{sed}=1900kg/m^3$. Then the difference of the gravity effect $\delta g = g_{sed}(\rho_{sed}) - \tilde{g}_{sed}(\rho\ (d))$ was examined from both grids (see Fig. 3.1.5). A difference of maximally $\delta g_{\max} = 2{,}4 \cdot 10^5 m/s^2$ is obtained whether a constant density or a variable density were used. The difference increases with increasing of the sediment thickness. Conclusively it is necessary to use a density –porosity function for computation of the density of sediments. Because by using of a constant density for the sediments, the error of calculation increase.

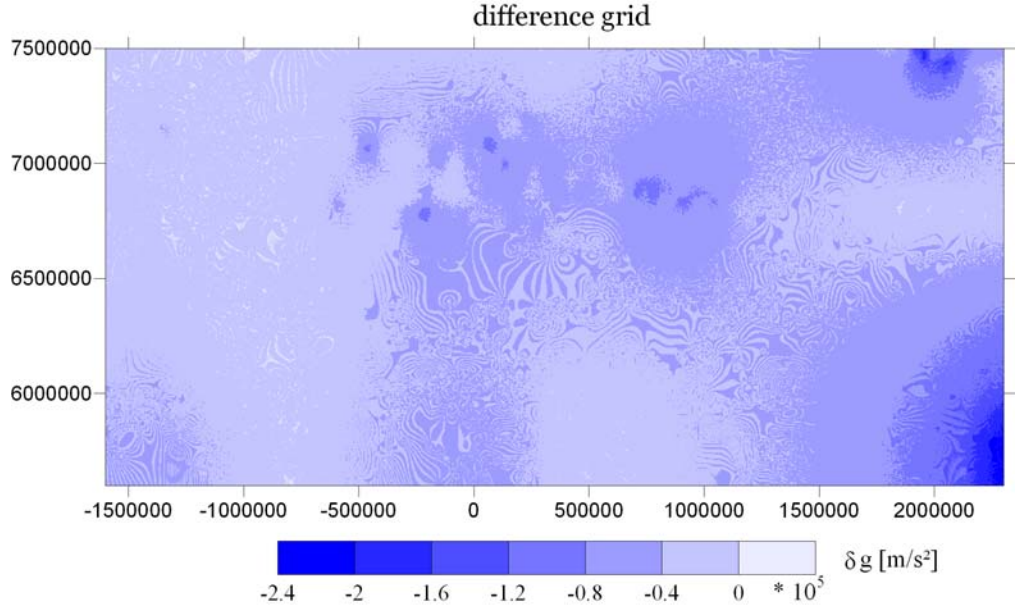

Figure 3.1.5) The difference was computed for the grids of gravity effect from Fig.3.1.4.

In a next step the gravity effect of sediments was subtracted from the Bouguer anomaly grid in the same area. Then from this reduced Bouguer anomaly grid the gravity CMI was estimated by gravity inversion according to Parker algorithm (see Chapter 1.3). The difference in the CMI depth after five iterations is presented in Fig. 3.1.6. As example the model for the reference depth $30km$ and density contrast $\Delta\rho = 500kg/m^3$ is chosen.

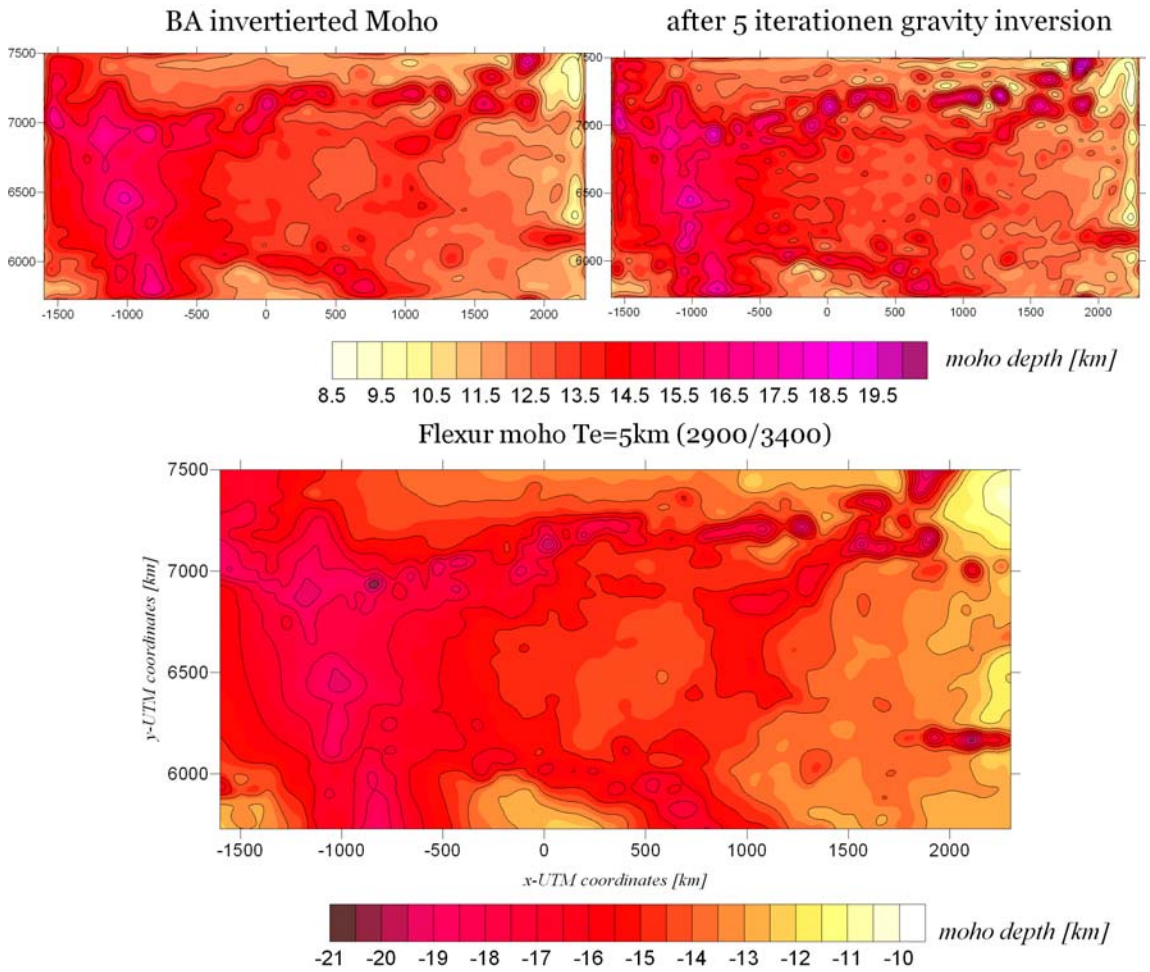

Figure 3.1.6) The Bouguer anomaly inverted CMI after 5 iteration step is similar to the flexure CMI calculated for $T_e = 5km$ and the same density contrast.

With increasing of the iteration step the CMI undulation under the seamounts increase. After 5 iteration steps the process can be finished, because I obtain no significantly differences for further iteration steps. The computation of the flexure CMI was done for the same parameter of density contrast $\Delta\rho = 500kg/m^3$ and reference depth $30km$. Furthermore an elastic thickness value $T_e = 5km$ was chosen. Except of the convention that the depth has positive values in the process of gravity inversion and negative value in calculation of the flexure, I obtain a similar result for the gravity and flexure CMI depth variation (Fig. 3.1.6). Similar depths of the CMI are obtained for the gravity CMI (Fig. 3.1.7), which was estimated for a reference depth $30km$ and density contrast $\Delta\rho = 450kg/m^3$. For both values of density contrast I obtain reproducible values for the CMI depth variation. Due to these observations both models of density contrast are used for further investigations.

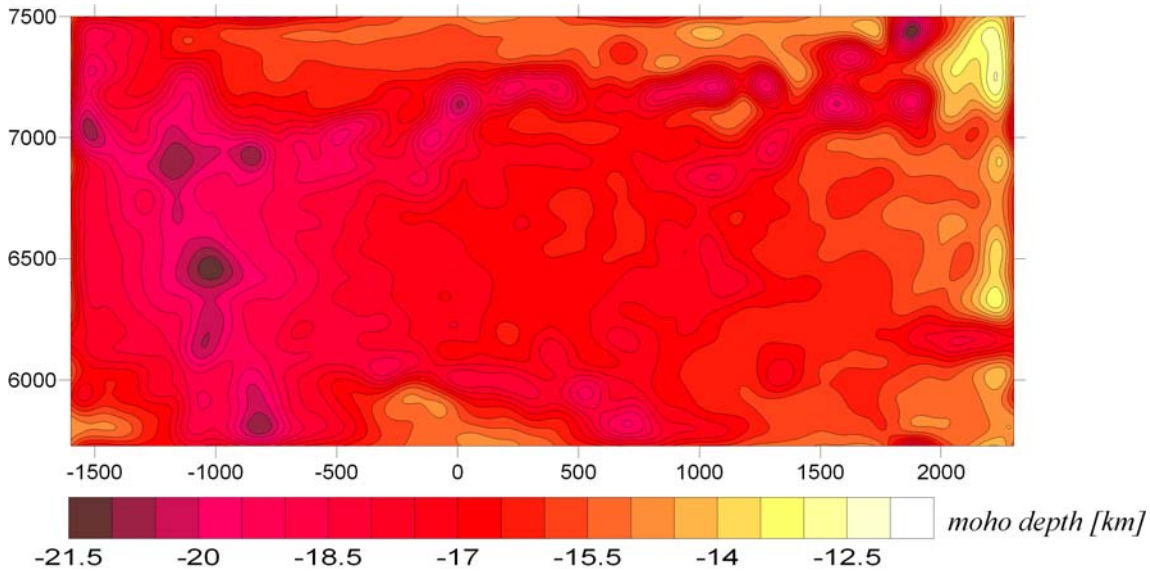

Figure 3.1.7) The gravity CMI depths variation was calculated for a density contrast $\Delta\rho = 450kg/m^3$.

3.1.4 Estimation of rigidity and elastic thickness

On square windows of side length $L = 60km$ for the first model and $L = 100km$ for the second model the difference of the gravity CMI and flexure CMI were calculated. The RMS difference between the two CMI surfaces is minimized by varying the elastic thickness Te (see Chapter 2.6).

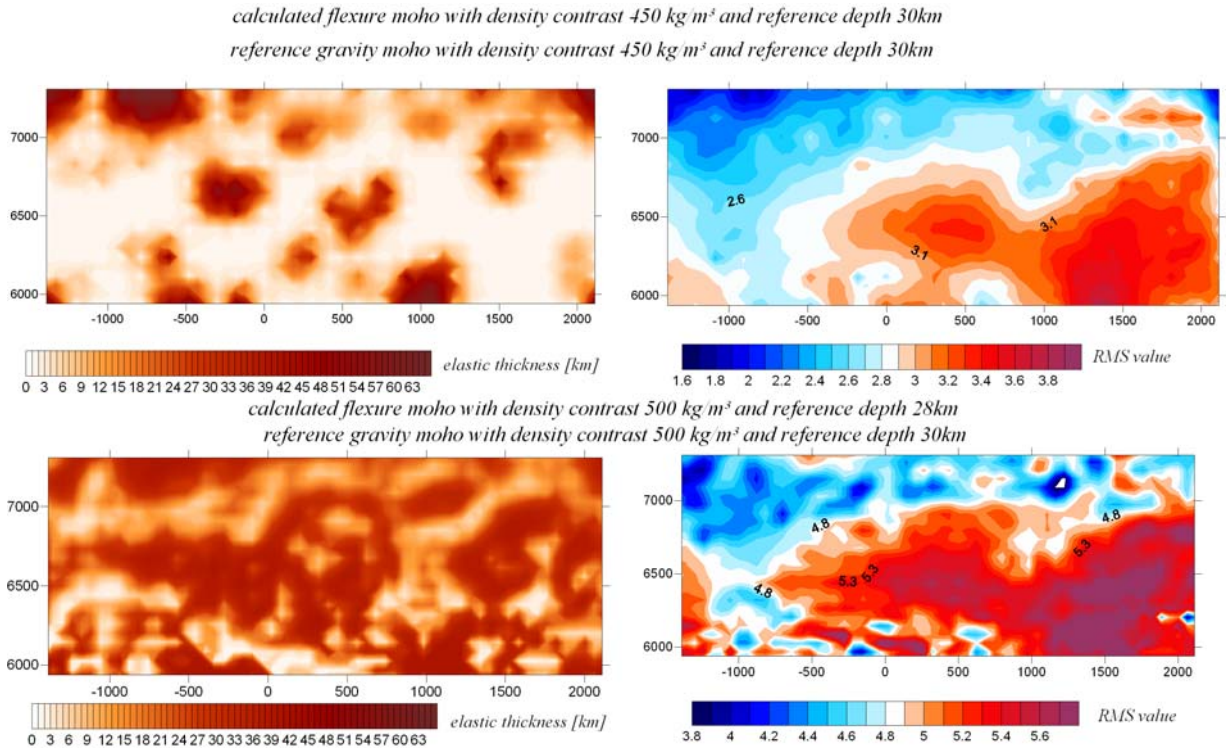

Figure 3.1.8) The elastic thickness variation and RMS value were estimated for different reference depth and density contrast.

The results are presented in Fig. 3.1.5 for the elastic thickness variation *Te* and the *RMS* value. In the first model the flexure CMI and the gravity CMI were estimated for the same parameter of density contrast $\Delta\rho = 450kg/m^3$ and reference depth $30km$.

In the second model the best result of T_e variation was obtained for a reference depth of $28km$. This value is $2km$ different from the reference depth used for estimation of the gravity CMI. The density contrast used for estimation of the gravity and flexure CMI have the same value of $\Delta\rho = 500kg/m^3$. By consideration of both results of T_e distribution I obtain comparable results. In the middle of the area the T_e values are high for both models. However, in the model 2 calculated for a density contrast $\Delta\rho = 500kg/m^3$ many values are $T_e = 1km$. The resolution of the distribution is lower compared to model 1 calculated with a density contrast $\Delta\rho = 450kg/m^3$. In view of the much higher resolution for the T_e distribution the model 1 is chosen in the following investigation.

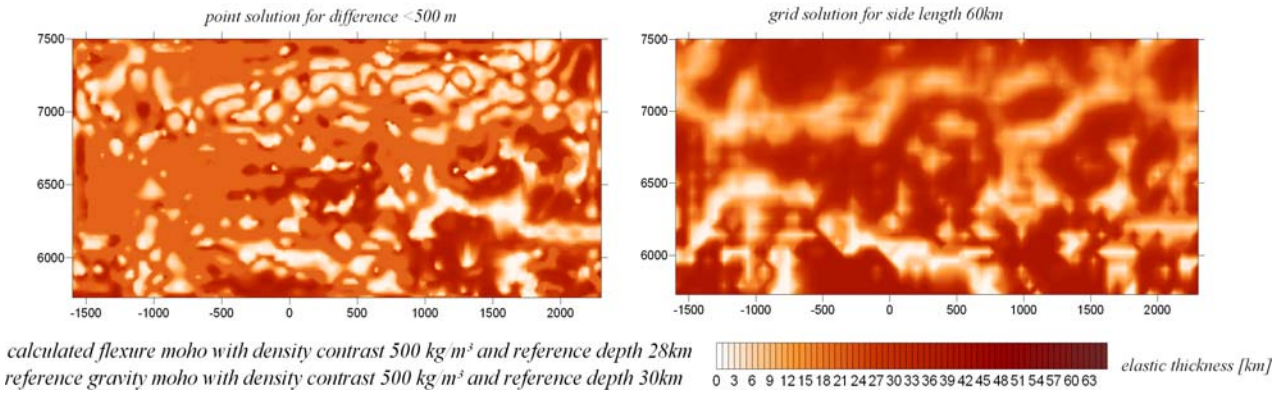

Figure 3.1.9) Comparison of elastic thickness variation for point solution and grid solution with side length $L = 60km$.

Considering the point solution (Fig. 3.1.6) similar results of T_e distribution are obtained, compared to the results for grids of side lengths $L = 60km$.

3.1.5 Discussion and conclusion

The solution of rigidity/elastic thickness was overlaid with the topography in the area of investigation and earthquakes. No relation is obtained between the earthquakes and the elastic thickness/rigidity distribution. However, I obtain in Fig. 3.1.7 a good correlation between lower elastic thickness values and the occurring of seamounts, especially in the area of the Sala y Gomez Ridge, the Nazca Ridge and the Juan Fernandez Ridge (JFR).

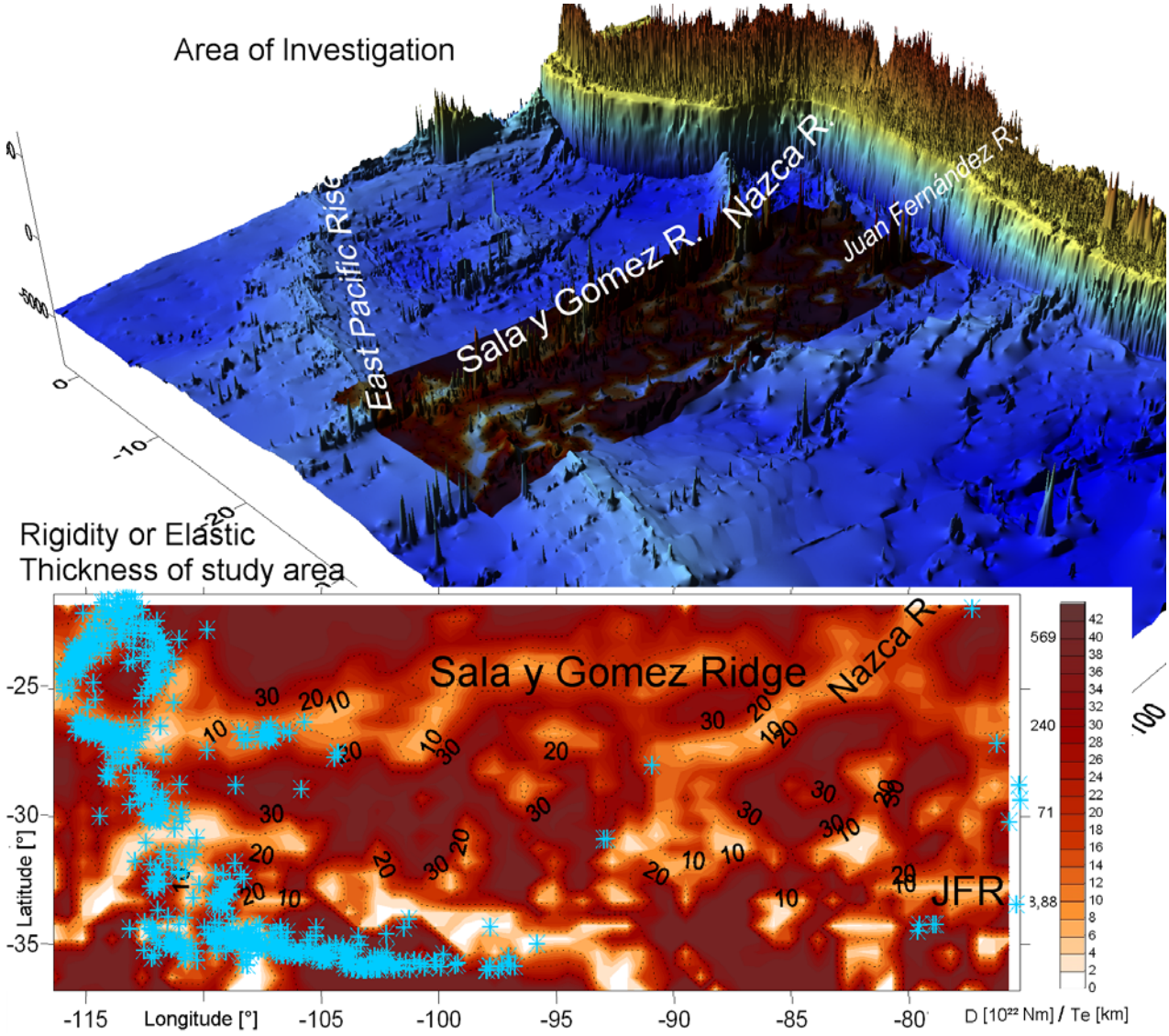

Figure 3.1.10) The elastic thickness/rigidity variation overlain on the topography and epicenters (marked in light blue).

The theoretical possibility of strength reduction beneath the mountains was already demonstrated by BUROV & DIAMENT (1992) for continents and by WESSEL (1993) for oceans. Even earlier, a number of authors mentioned such an effect from direct observations of flexure (e.g. ZOETEMEIJER ET AL.1990, ABERS & LYON-CAEN 1990). It is also shown that a high topography is able to create large zones of brittle failure in adjacent regions (BUROV & DIAMENT 1995), usually associated with shallow seismicity. These considerations are consistent to my results.

Furthermore a structure of lower rigidity can be recognized in Fig. 3.1.7, which proceeds in north/west direction from $-90°Lon$ colloquial $-30°Lat$. This structure will be investigated in the following. Therefore a map of fault and structure zones proposed by LAWVER & SANDWELL (1990) was overlain on the results of elastic thickness distribution.

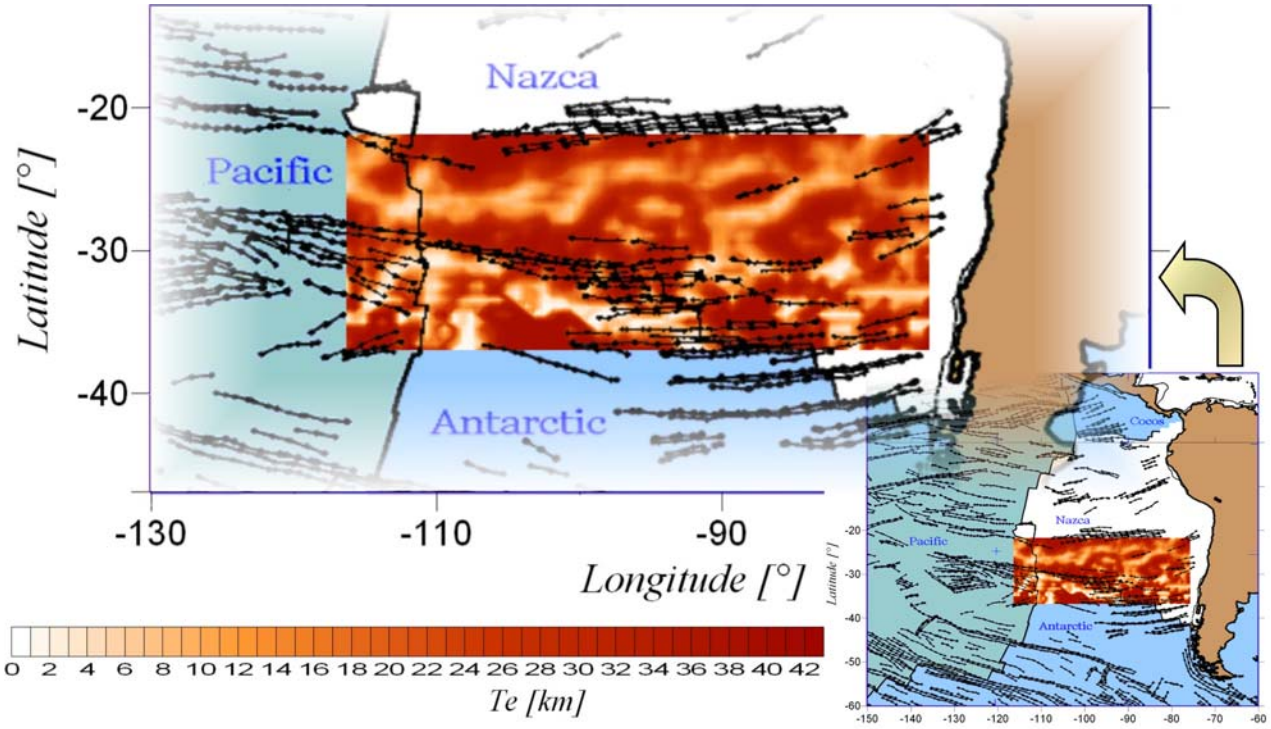

Figure 3.1.11) The fault structures and fault zones in the Pacific Ocean, overlain on a map of elastic thickness variation. Between higher values of elastic thickness and faults is a good correlation observed.

This structure is obviously coincident with the Antarctic-Nazca plate boundary, characterized by lower T_e / D values (Fig. 3.1.8), which are caused by an increased heat flow and crustal thinning (PERS. COMM. NOGEIZIG). The mid-oceanic triple junction of the Pacific-Antarctic-Nazca plate is as well characterized by lower T_e / D values. Within the Antarctic plate higher values are obtained, as well as between the Nazca ridge and the JFR. These rigid parts are surrounded by crustal areas of lower T_e / D values, which might indicate the existence of micro-plates as proposed by TEBBENS ET AL. (1997).

A good correlation between the fault structures and the T_e / D distribution is observed. The faults are located in the transition zone between higher and lower T_e / D values (PERS. COMM. KOLLERSBERGER). The direction of the faults correlates with the direction of the T_e / D transition zones. It would be instructive to express this visual correlation quantitatively and to test it against some random patterns (PERS. COMM. HEUBECK). This is a task for further investigations.

3.2 CENTRAL ANDES

3.2.1 Input data

The gravity database was collected by field measurements and offshore shipboard campaigns as described by GÖTZE & THE MIGRA GROUP (1996). A 3D density IGMAS model by KIRCHNER (1997) was used in order to obtain the pseudo topography and the CMI depth variation (see Fig. 3.2.1). The pseudo topography (Chapter 1.4) was calculated with the external and internal loads by Schmidt (PERS. COMM. SCHMIDT).

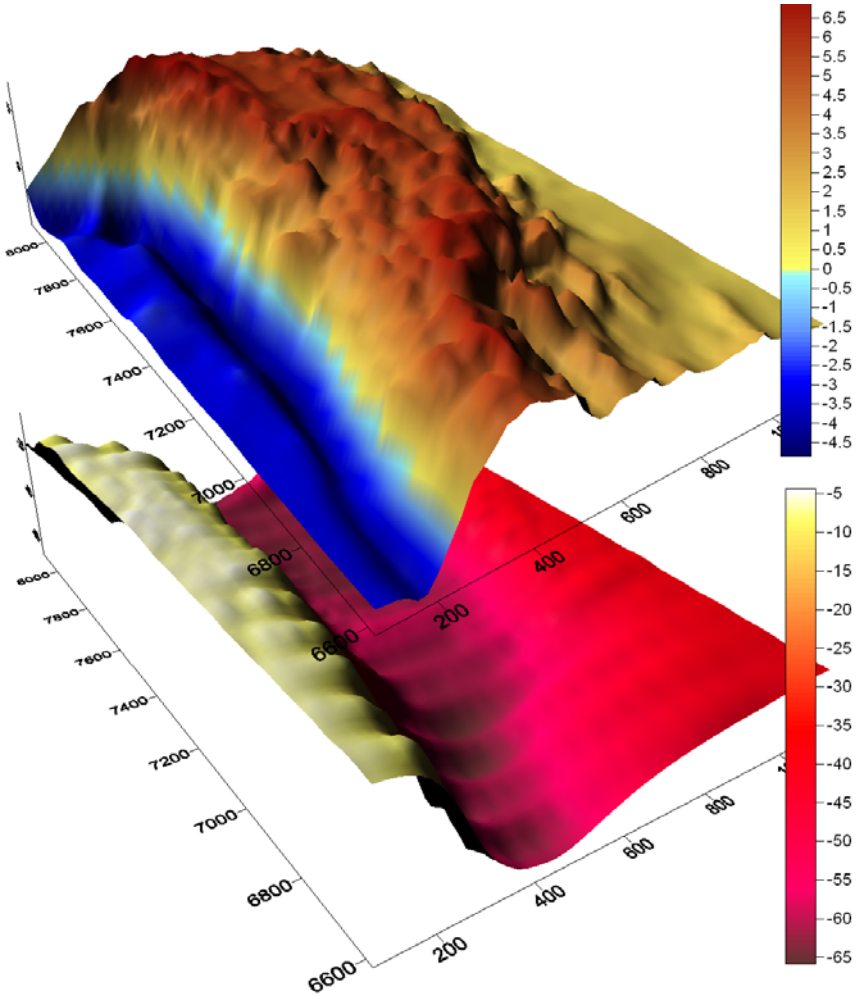

Figure 3.2.1) Pseudo topography in $[m]$ and CMI depth in $[km]$ is obtained from IGMAS modeling for UTM coordinates in $[km]$.

The size of the area of the pseudo topography is equal to the area of the reference CMI. Due to the calculation process (see Chapter 2.6), the area of the results becomes smaller by the radius of convolution corresponding to the maximum T_e (e.g. $R \approx 500km$ for $T_e = 60km$).

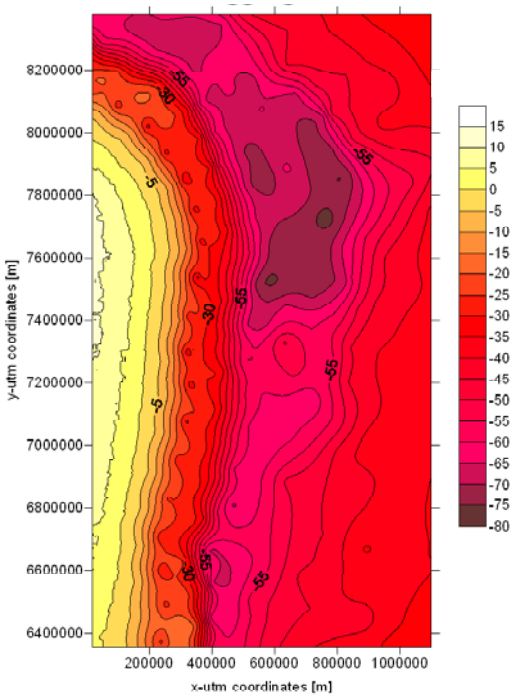

Figure 3.2.2) The CMI depth $[km]$ was obtained from IGMAS modeling for UTM coordinates $[m]$.

Additionally, a new 3-D IGMAS density model by TASSARA (PERS. COMM.) provides a reference CMI (Figure 3.2.2).

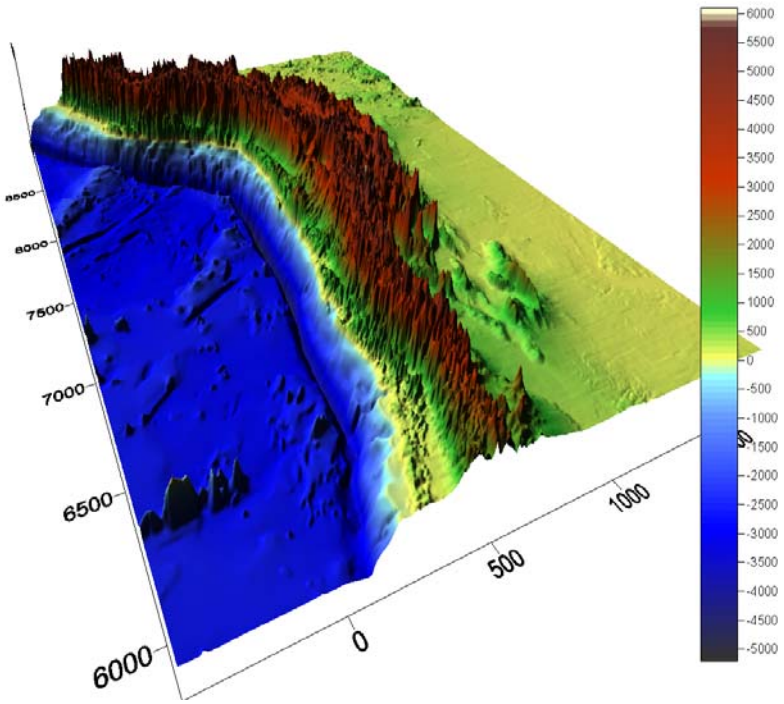

Figure 3.2.3) Topography and bathymetry $[m]$ in UTM coordinates $[km]$ from NOAA/GEBCO was used to calculate a load model of Central Andes, which was used for the computation of flexural rigidity.

For this second model the topography/bathymetry from GEBCO/NOAA was used as input grid. This was transformed to a so called "load model", which means that every point of the input grid with a coordinate $z < 0$ has to be multiplied with the factor $\frac{(\rho_c - \rho_w)}{\rho_c} = 0.645$ for an assumed density of the crust $\rho_c = 2900 kg/m^3$ and the density of water $\rho_w = 1030 kg/m^3$. Thereby the area for the input topography has to be larger than the area of investigation by the amount of the radius of convolution referring to the maximum elastic thickness value (see chapter 2.6). Figure 3.2.3 presents the load model of the Central Andes. Comparing both input grids the maximum height of the pseudo topography is higher than that of the load model by the amount of $h = 1000m$, caused by the mass surplus. For both models the distribution of T_e and D have been estimated.

3.2.2 Preliminary investigation

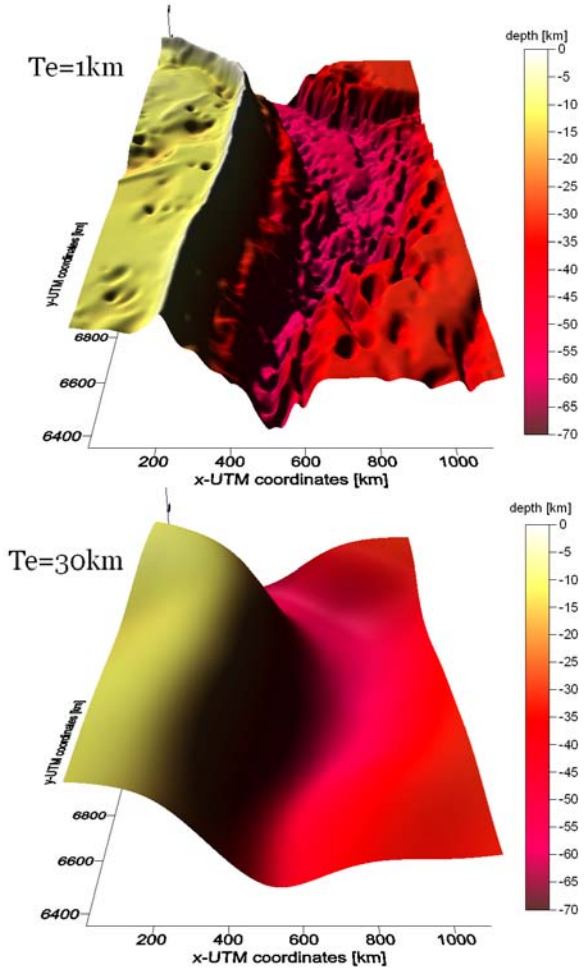

Figure 3.2.4) The two flexure CMI's were calculated for load model of Central Andes for $T_e = 1km$ and for $T_e = 30km$.

The flexure CMI's presented in Fig. 3.2.4 were computed with the analytical solution for the load model with a reference depth $30km$, density of crust $\rho_c = 2900 kg/m^3$ and density of

mantle $\rho_m = 3380 kg/m^3$. The CMI referring to $T_e = 1 km$ is strongly undulated. The CMI referring to $T_e = 30 km$ is less deflected. The maximum depth is located below the Andean orogen and reaches up to a value of $70 km$.

The flexure CMI's, estimated for the pseudo topography (Fig. 3.2.5), were calculated by the analytical solution with a reference depth $40 km$, density of crust $\rho_c = 2900 kg/m^3$ and density of mantle $\rho_m = 3380 kg/m^3$. Comparing the flexure CMI calculated for $T_e = 22 km$ (as an average value for elastic thickness) with the reference CMI a difference in the maximum depth of $10-15 km$ is obtained (Fig. 3.2.5). In view of the fact that the CMI surfaces show the same flexural behavior but their maximum depth is different, another reference depth of $30 km$ is chosen.

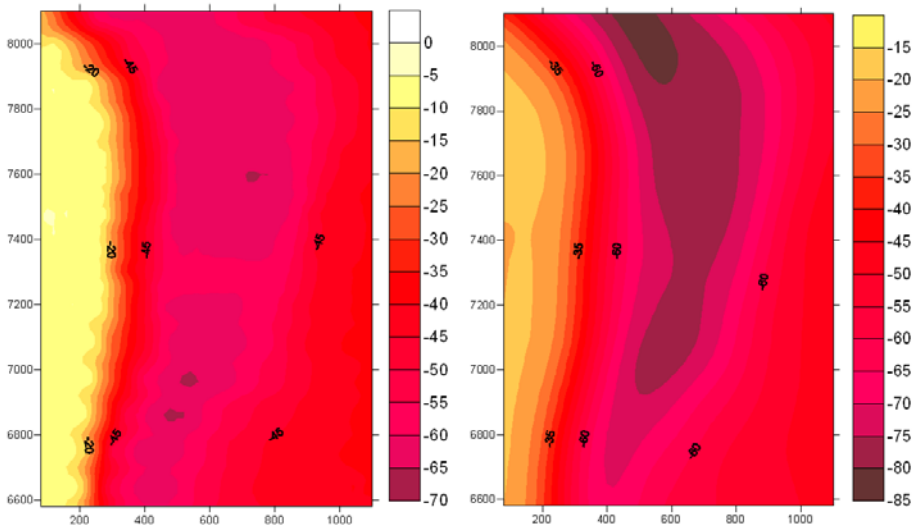

Figure 3.2.5) The reference CMI derived from IGMAS (right side) is compared with a flexure CMI calculated for pseudo topography (left side) of Central Andes for $T_e = 22 km$ and a reference depth $40 km$. The maximal CMI depth of both CMI's is $10-15 km$ different.

3.2.3 Estimation of rigidity and elastic thickness

As described in Chapter 2.6, the elastic thickness/flexural rigidity distribution was calculated for the parameters side length $L = 60 km$ and reference depth $30 km$ in both models. The results are presented in Fig. 3.2.6 for the elastic thickness variation T_e obtained for the load model; Fig. 3.2.7 presents the results for the pseudo topography. The T_e / D distribution obtained for the load model are characterized by lower T_e / D values in the area of the volcanic arc and the Andean orogen (Fig. 3.2.6), the oceanic plate shows parts of lower T_e / D values as well. The area of the coast line is characterized by high T_e / D values. In the area of Salta-Jujuy and Tarija a rigid body can be obtained, as well in the area of Catamarca. The

area between $29-33°S/64-67°W$ is dominated by high T_e/D values. In La Rioja is a small local area of low elastic thickness.

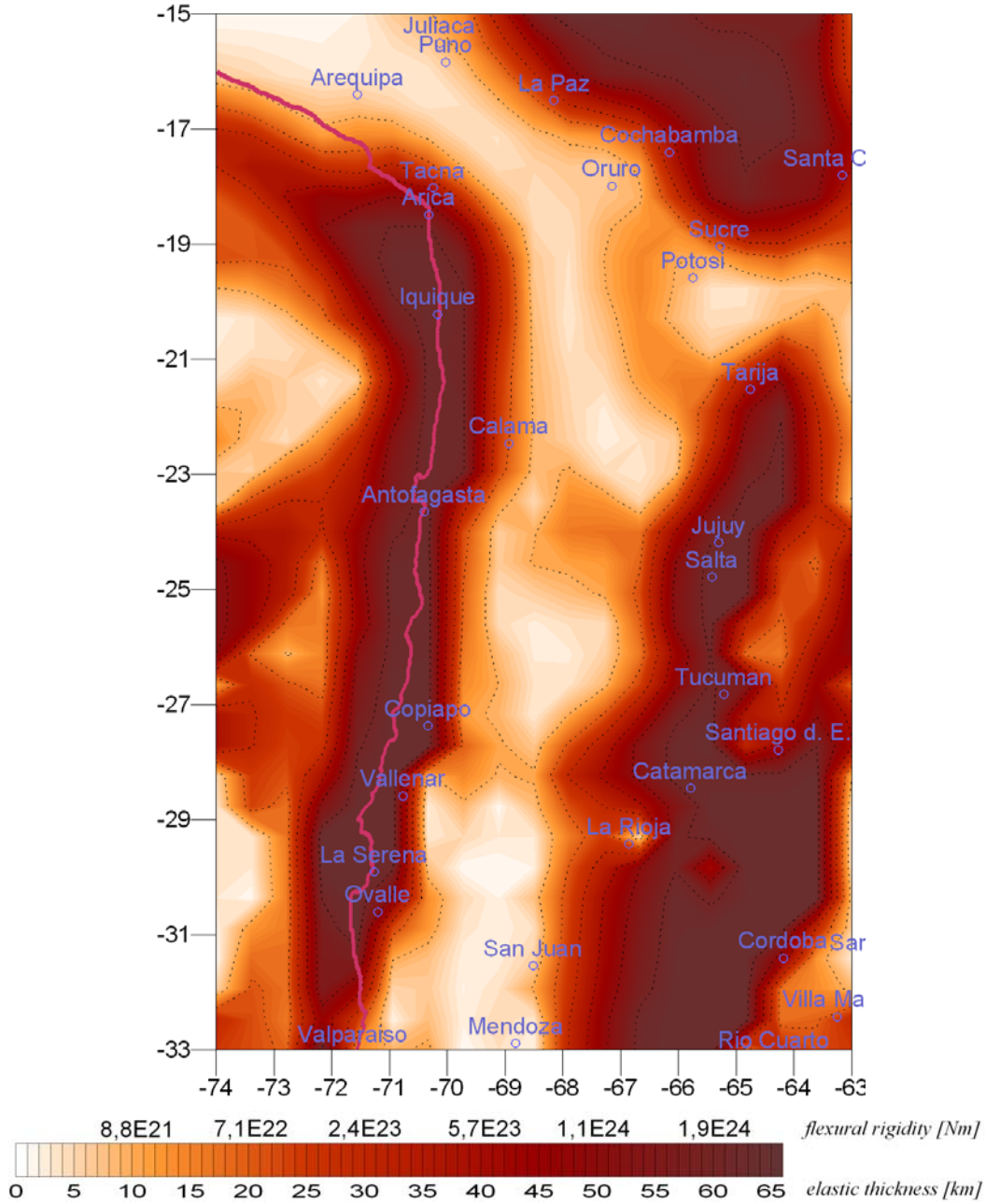

Figure 3.2.6) The distribution of flexural rigidity/elastic thickness was estimated for the load model and a reference depth $30km$.

The results for the pseudo topography (Fig. 3.2.7) shows in opposite to the load model higher T_e/D values in the area of the Andean orogen ($70-67°S$).

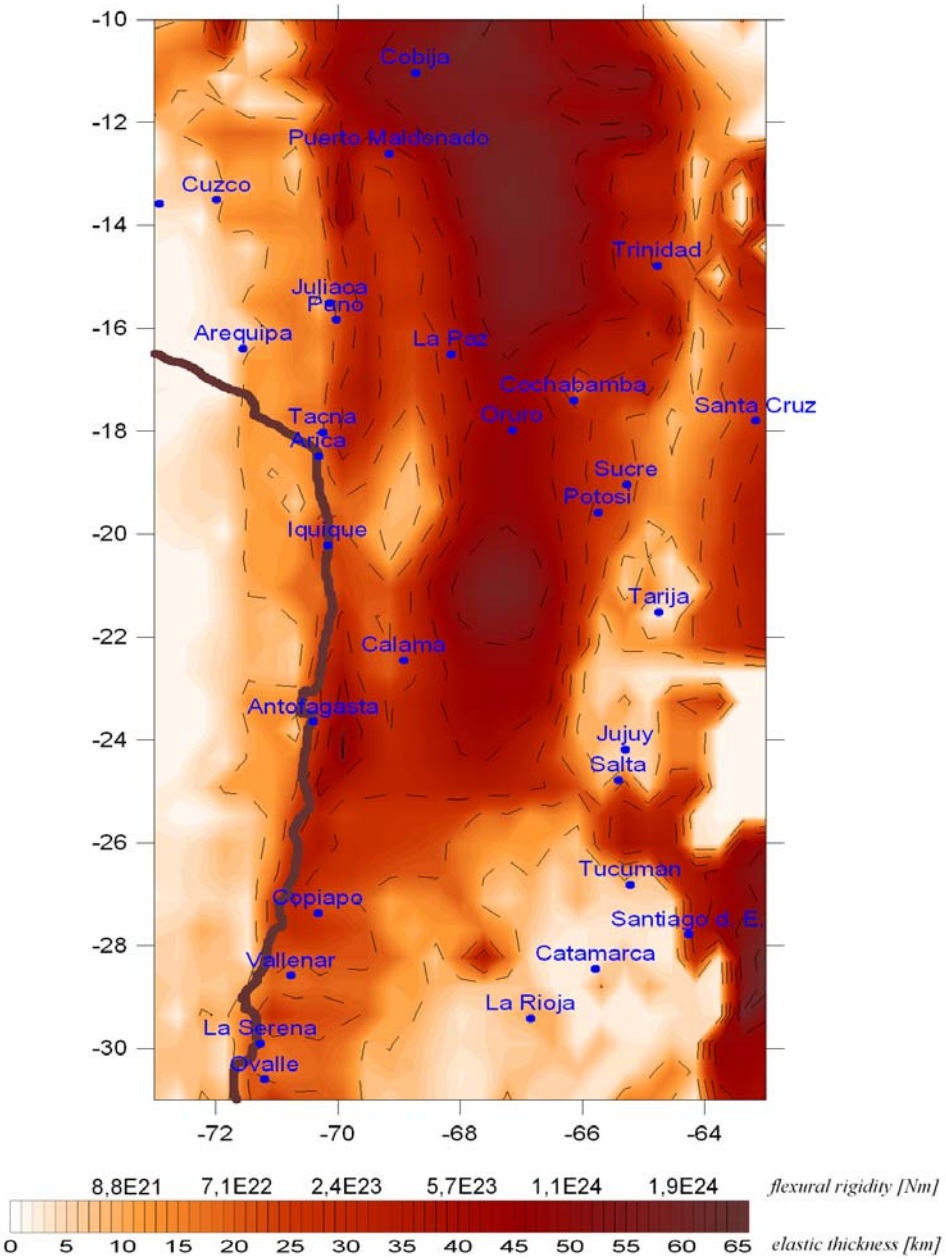

Figure 3.2.7) The distribution of flexural rigidity/elastic thickness was estimated for the pseudo topography and a reference depth $30km$.

Regional different T_e / D distribution is obtained compared to the results calculated for the load model. The oceanic plate is characterized by low T_e / D values. In the area of Salta-Jujuy and northwards low T_e / D values occur, this results correlates not with the results from the load model. However, I find some similarities between the results, for example, in the area of Salta-Jujuy and Tucuman, the higher elastic thickness values indicate a rigid structure.

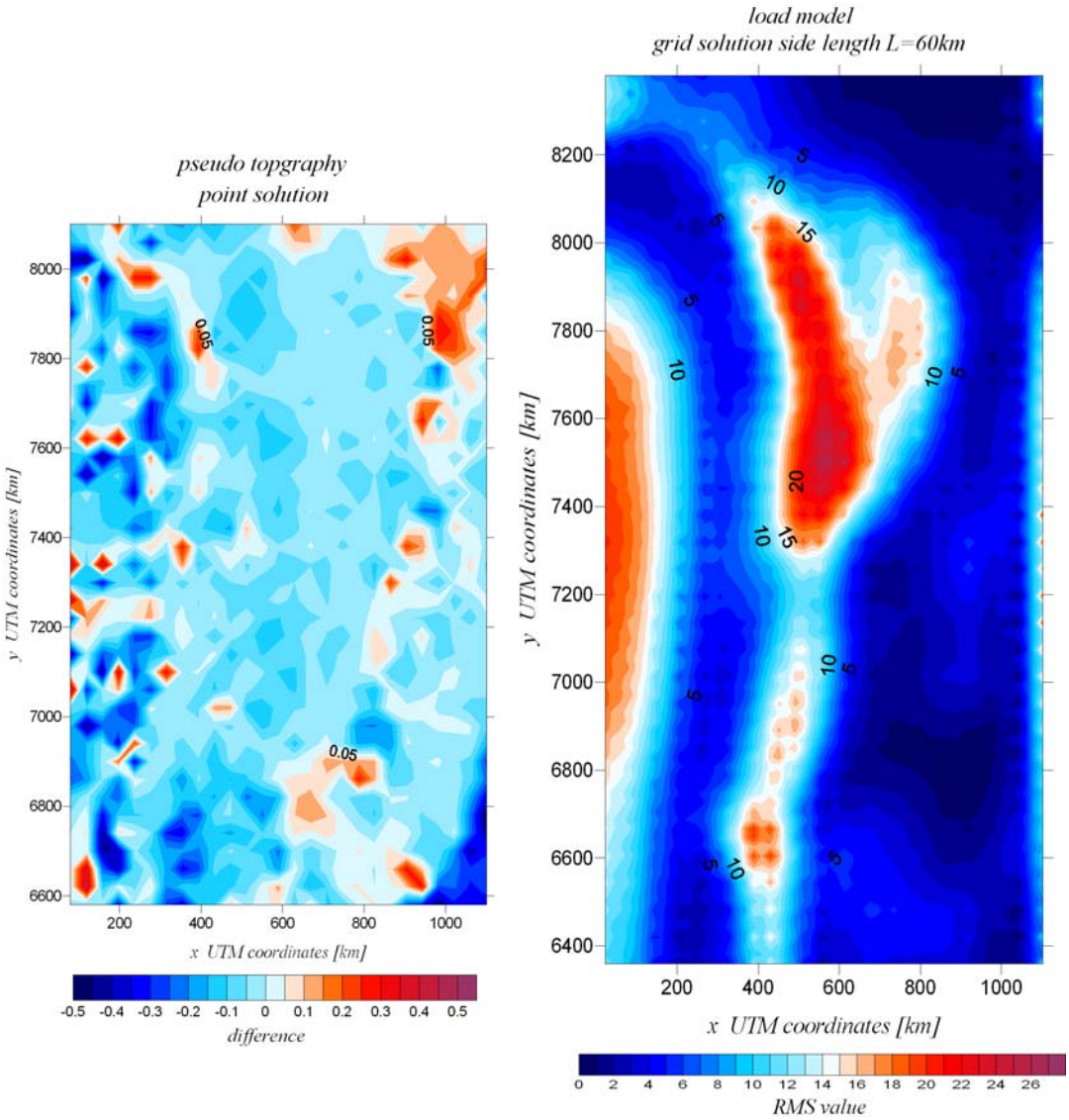

Figure 3.2.8) The differences between the flexure CMI and reference CMI are compared for pseudo topography and load model of Central Andes.

By comparison between the calculated flexure CMI and the reference CMI of the load model and the pseudo topography I obtain a good regional fit. The RMS difference is shown in Figure 3.2.8 for both models. I obtain a very good fit for the pseudo topography. The flexure CMI is in agreement with the gravity CMI with differences smaller than $\Delta w \leq 500m$ for a point solution. Higher RMS values occur in the load model, smaller than $6km$ predominantly. The following chapter shows that the point solution and the grid solution provide similar results for the spatial variation of T_e / D.

3.2.4 Discussion and conclusion

Rigidity and elastic thickness have been calculated with the coherence method in the area $21{,}5°S - 28°S$ by KÖSTERS (1999). For each squared grid of the side length $L = 340km$ a constant elastic thickness or rigidity were estimated due to the comparison of observed

coherence and calculated coherence. I compare his results of the coherence method with the results of the analytical solution (Fig. 3.2.9). In view of easier comparison of the results for pseudo topography and load model, the area is cut in the same size and the estimated values are colored by similar color scale. In a global view the results for the load model are similar to the results of the coherence method.

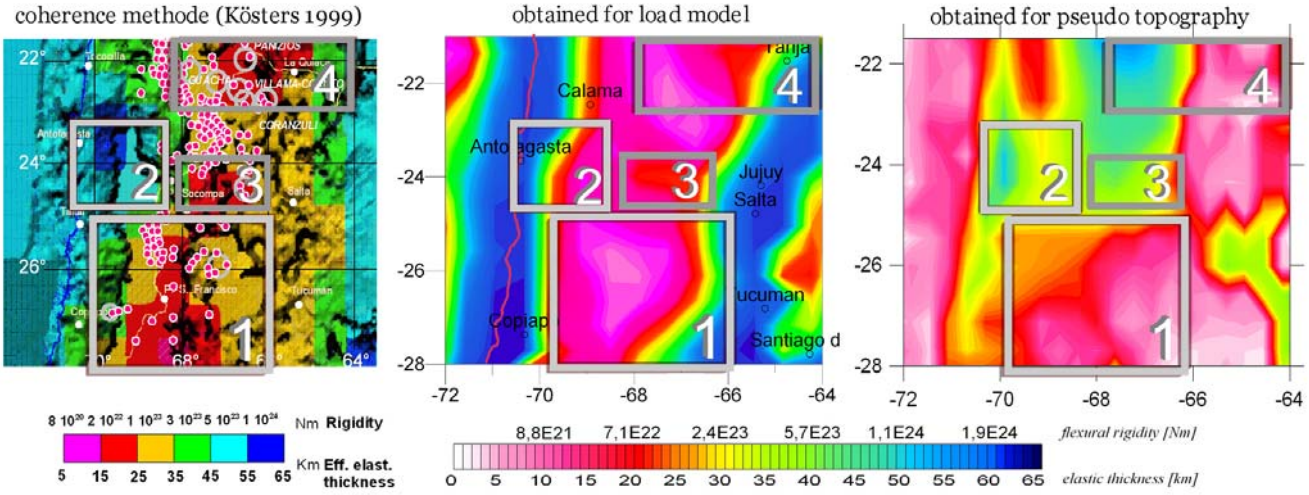

Figure 3.2.9) The results of coherence method are compared with the analytical solution for pseudo topography and load model of Central Andes.

In the area of the volcanic arc the T_e / D values are smaller. The area of the coastline is described by higher T_e / D values, in opposite to the results of the pseudo topography. In a local view a good correlation can be find between the results of pseudo topography, load model and coherence method in the area $70°W - 66W / 28°S - 25°S$ (marked in Fig.3.2.9 with gray box Nr.1). This area is characterized by lower Te-values in the range of $T_e = 5...25km$.

In the local area $68{,}5°W - 66W / 25°S - 24{,}5°S$ and $68°W - 64W / 22{,}5°S - 23°S$ the results are similar for the load model and the coherence method (marked with gray boxes Nr 3 and 4). In those parts of Andean orogen occurs lower T_e values. These results are in opposite to the results of pseudo topography, where a high rigid body with $T_e \geq 40km$ is estimated. On the other side in the local area $71{,}5°W - 68{,}5W / 25°S - 23°S$ the results from the coherence method is similar to the results of pseudo topography (marked with gray box Nr 2). High values of $T_e \approx 45km$ are estimated. In the case of the load model the same area is described by lower T_e values.

In view of the fact that KÖSTERS used $E = 100MPa \equiv 10^{11} Nm$ as standard value for the Young's modulus, the rigidity values are different, but the elastic thickness values should be the same. He used for estimation of the elastic thickness values the pseudo topography and CMI depth from the IGMAS model by KIRCHNER (1997). But although the same input data are used, the results are not similar to the results for the analytical solution estimated for the pseudo topography.

Therefore I discuss the results in view of the reference depth and grid side length, because these parameters are different and might lead to a different result in elastic thickness distribution. Concerning the reference depth (see chapter 2.6, Fig. 2.6.8) I conclude that a variation of $\pm 10km$ in reference depth has not much influence on the result. Therefore, the difference in reference depth does not cause the difference in the T_e distribution.

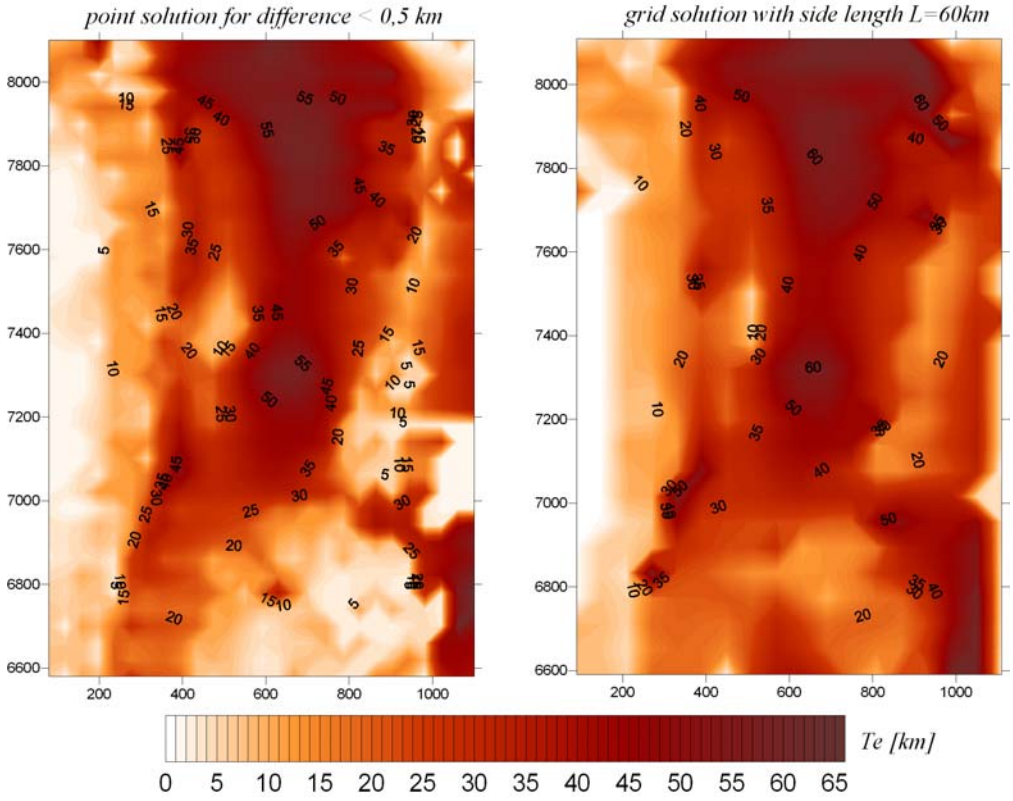

Figure 3.2.10) The results for pseudo topography of Central Andes are compared for point solution and grid solution with side length $L = 60km$.

Comparing the results for the point solution with the grid solution with $L = 60km$, a similar T_e distribution is obtained (Fig.3.2.10). Additionally Chapter 2.6 (see Fig. 2.6.7) shows that for a side length $L = 60km$ or $L = 340km$ only the resolution for T_e distribution is changing. Therefore the differences in T_e distribution calculated for pseudo topography is not caused by the difference in side length.

It is still questionable why the T_e distribution estimated by KÖSTERS IS different, although the same pseudo topography was used. It cannot be caused by an error in calculation with the analytical solution, because I compared the solution with the FFT techniques, for the Airy solution and the Vening-Meinesz solution. This should be sufficient for an evidence for correct calculation. It is a task for further investigation to explain the differences in the results of the T_e distribution. Therefore it is necessary to estimate the T_e distribution in the Central Andes with different methods and to compare all results.

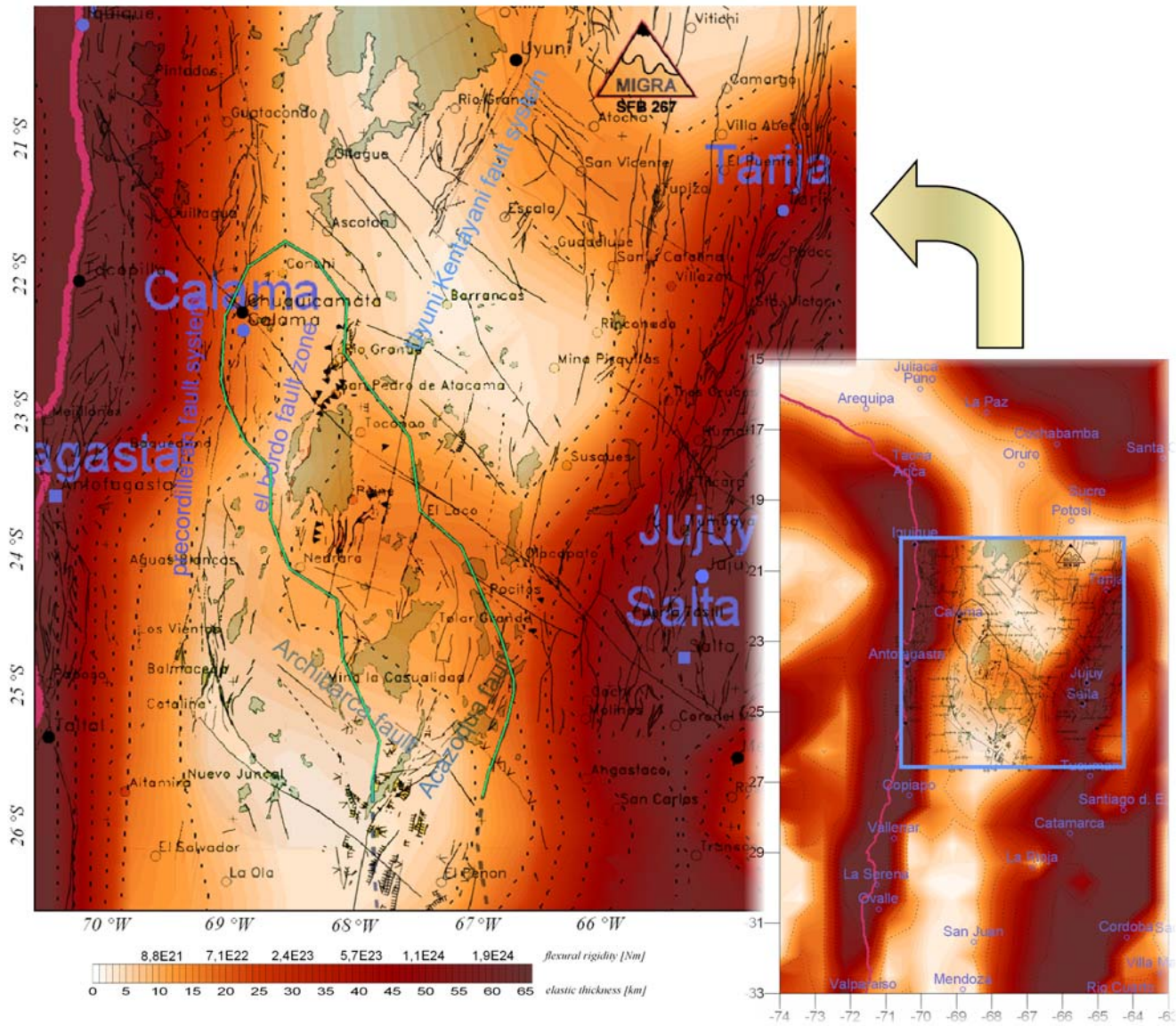

Figure 3.2.11) The T_e and D results for load model of Central Andes are overlain with geological lineaments, salt lakes and outline of CAGH in green (overlay source: Götze & Krause 2002)

Nevertheless, in the following I concentrate on the results for the T_e distribution obtained for the load model. Fig. 3.2.11 shows the results compared with the faults structures and the position of the Central Andean Gravity High (short: CAGH). The CAGH was discussed in many articles in view of its evolution and structure and it corresponds to a seismic high-velocity zone, which is located at shallower depths (e.g. BAHLBURG & HÉRVE 1997, LESSEL 1998, LUCASSEN ET AL. 1999). Also SCHURR (2001) conducted tomographic studies in the region of the CAGH and obtained high seismic velocities. GÖTZE & KRAUSE (2002) supposed the role of the dense rocks of the CAGH as driving factor for the direct control on the location of fault zones and style of deformation in this region. Thereby the CAGH is a positive anomaly in the isostatic residual gravity field for a mean rigidity of $D = 10^{23} Nm$. The numerical investigation of the gravity anomalies of the CAGH indicates a $400km$ long and

$100-400km$ wide dense body, which is located in a depth of $z \cong 155km$. The CAGH is limited by the West Fissure/Limon Verde fault system in northwest and by the "El Bordo" and the Uyuni - Kentayani fault system in southeast. The geological lineaments, salt lakes and location of CAGH presented by GÖTZE & KRAUSE (2002) from the data bank of the SFB 267 were overlain with the elastic thickness/rigidity distribution obtained from the load model.

I obtain a very good correlation between the location of the CAGH (green colored in Fig. 2.3.11) and the presence of a more rigid body related to the surrounding area of Andean orogen globally characterized by lower T_e / D values. Additionally I observe a very good correlation between the direction and the location of the faults and fault systems. The Archibarca fault is located between the border of a rigid and softer zone of crust predicted by the T_e / D values. Predominantly the faults are located in a transition zone between high and lower T_e / D values. The fault systems located near Antofagasta correlate well with the area of a rigid crust predicted by high T_e / D values. As well the faults originating at Jujuy/Salta and the ones situated near Tarija, which proceeds in north-west direction correlate well with the area of a rigid crust described by higher T_e / D values.

In general a good correlation is obtained between the T_e / D distribution and the direction and location of the faults. Because the location and direction of faults are independent information, this is another evidence for the analytical calculated results for the description of rigid and softer parts of the lithosphere. However, an investigation of the precision of T_e / D distribution and the method is discussed in Chapter 4. In the following chapter I apply the analytical solution in the Southern Andes.

3.3 SOUTHERN ANDES

3.3.1 Input Data

The gravity database has been collected by field measurements as described by GÖTZE ET AL. (2001) analyzed and interpreted by WIENECKE (2002). The gravity field studies were extended to the crustal density structure by an IGMAS modeling by TAŠÁROVÁ ET AL. (2003) and compared with results from the geological sciences by HACKNEY ET AL. (PERS. COMM.). Fig. 3.3.1 shows the pseudo topography and the gravity CMI achieved by IGMAS modeling (TAŠÁROVÁ 2005).

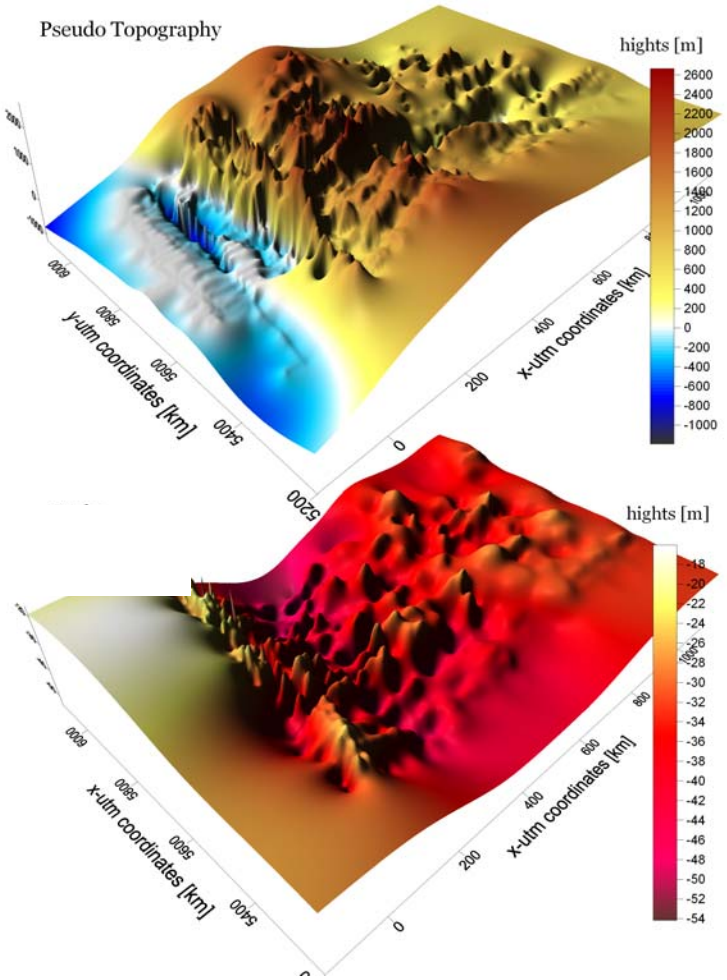

Figure 3.3.1) Pseudo topography and gravity CMI were obtained from the IGMAS modeling.

The size of the model area of pseudo topography does not allow a convolution radius greater than $R = 200km$. However, for calculation an elastic thickness value of $T_e = 65km$ a radius of convolution $R \approx 500km$ is required. For this reason the results for T_e / D distribution are include some uncertainties.

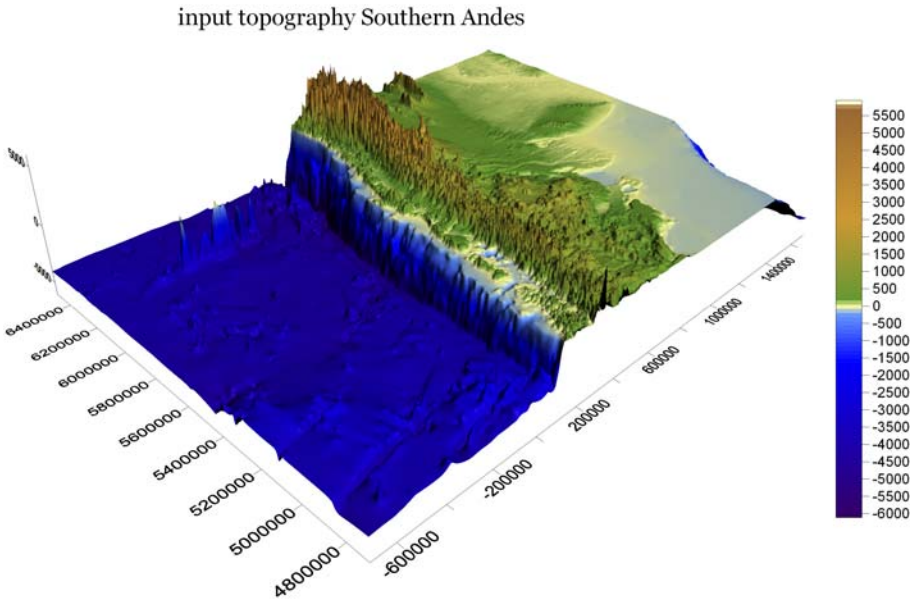

Figure 3.3.2) Input topography from GEBCO data was used to calculate the load model.

I also calculate the T_e / D distribution for a load model, using a $500km$ extended topography presented in Fig. 3.3.2 from GEBCO. The load model is calculated with a density of $\rho_c = 2800kg/m^3$ and a water density $\rho_c = 1030kg/m^3$.

3.3.2 Estimation of rigidity and elastic thickness

As described in Chapter 2.6 the flexure was calculated with the analytical solution for both models for the parameter: side length $L = 60km$ and reference depth $30km$.

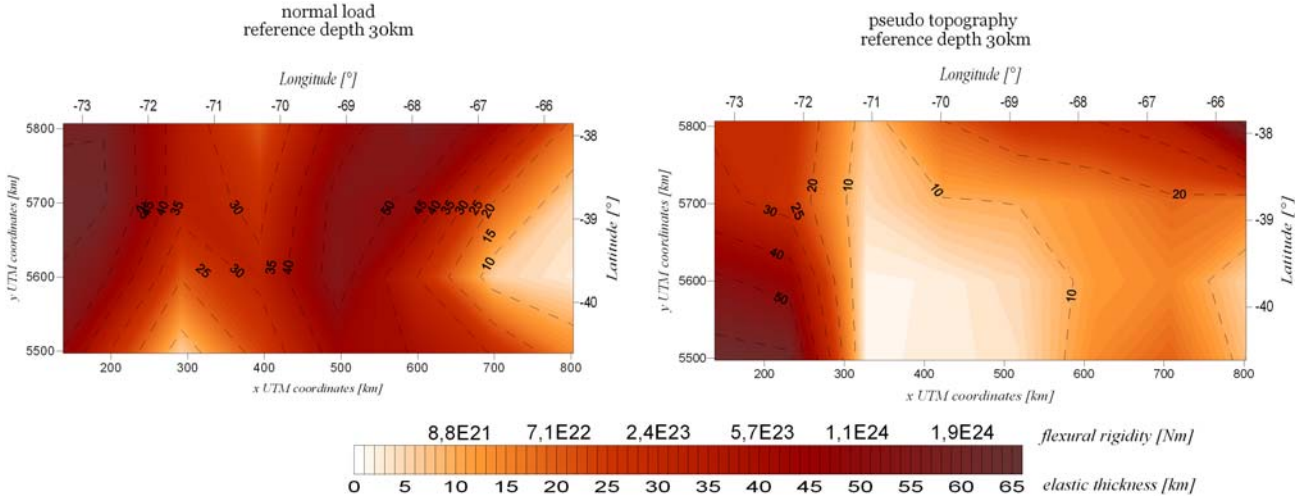

Figure 3.3.3) The flexural rigidity/elastic thickness distribution was calculated for the load model (left side) and pseudo topography (ride sight).

The T_e / D distribution is obtained by minimizing the difference of gravity and flexure CMI by varying the elastic thickness T_e. The results presented in Fig. 3.3.3 show similarities. The

eastern part of the area is dominated by low T_e / D values, the western part by higher values for both models. The central part of the study area is different. I obtain lower T_e / D values for the pseudo topography ranging from $1km \leq T_e \leq 15km$. In opposition to that the T_e / D distribution in the central part estimated for the load model is characterized by values between $15km \leq T_e \leq 45km$. In order to discuss the results I investigate the agreement of flexure CMI and reference CMI from IGMAS modeling. The difference between the gravity CMI and flexure CMI is shown in Fig. 3.2.4 for both models.

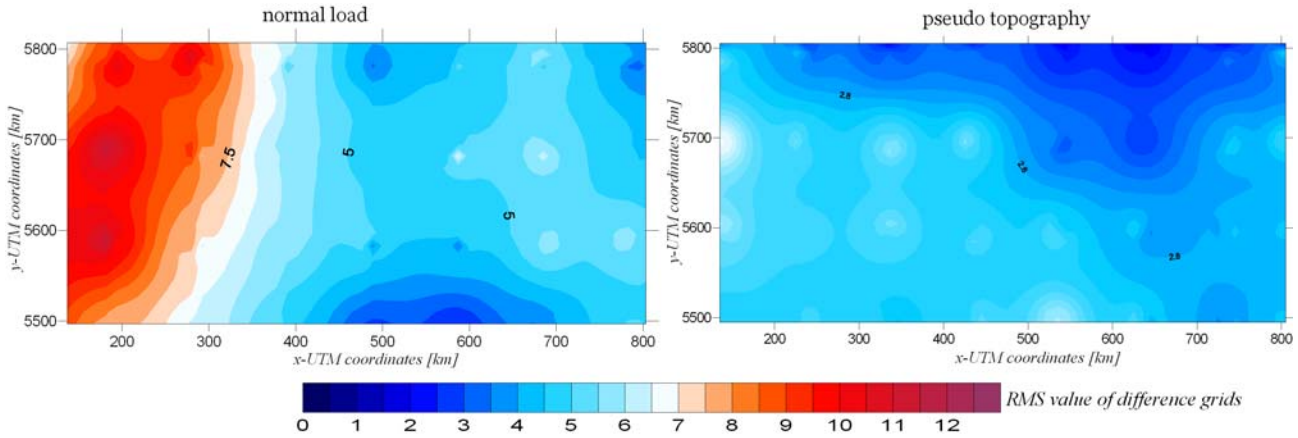

Figure 3.3.4) RMS value distribution for difference of flexure CMI and reference CMI was computed for load model (left side) and pseudo topography (ride sight).

By consideration of the distribution of *RMS* values I conclude that the agreement between the CMI's is more suitable for the concept of pseudo topography. In the load model high discrepancies occur in the western part of the study area. This is due to the fact that the effect of the slab is not considered in the load model but in the reference CMI. Therefore I obtain high *RMS* values in the offshore area. Predominantly the *RMS* value is $5km$.

3.3.3 Discussion and conclusion

The *RMS* values for pseudo topography (see Fig. 3.3.4) result in small circular shaped bulges . This is due to the fact, that the reference CMI is strongly undulated. In addition the area of pseudo topography is too small for T_e / D investigations, consequently the precision for the T_e / D distribution is to small and edge effects had to be included. The choice of reference depth for the load model is questionable, due to the predominant *RMS* value of $5km$. Therefore I recalculate the T_e / D distribution represented in Fig. 3.3.5 with a $5km$ shifted reference depth of $35km$. The results for the models of different reference depths are equal for the western part of study area, but differ for the central and eastern part. In both models the values of the elastic thickness/flexural rigidity range lower for the central part of the area of investigations. The result for the model with $30km$ reference depth shows a local anomaly of low T_e / D values in the eastern part, but this anomaly disappears if a reference depth of $35km$ is used in the calculation.

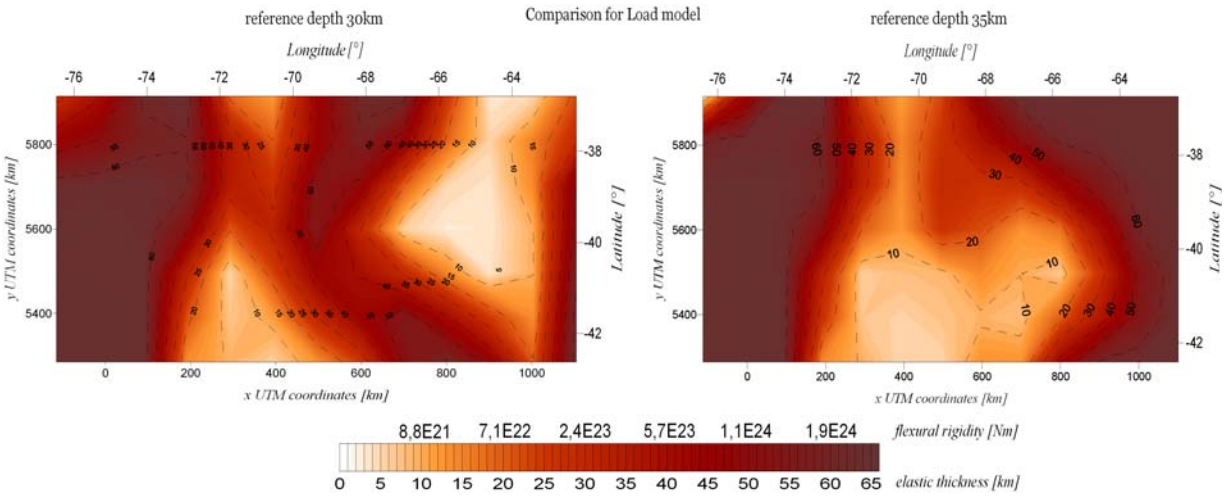

Figure 3.3.5) The flexural rigidity/elastic thickness distribution was calculated for load model with a reference depth $30km$ (left side) and reference depth $35km$ (ride sight).

This proves the importance of a suitable choice of the reference depth, regarding a local interpretation of the T_e / D distribution. Furthermore, using a reference depth of $35km$ produces similar results in the load model and in the pseudo topography model. Additionally it is more convenient to receive higher values of T_e / D for the eastern part of the study area, since a rigid craton is located in the northeast (see Fig. 3.3.8). This is the reason for interpreting the results for the model using a reference depth of $35km$ in the following.

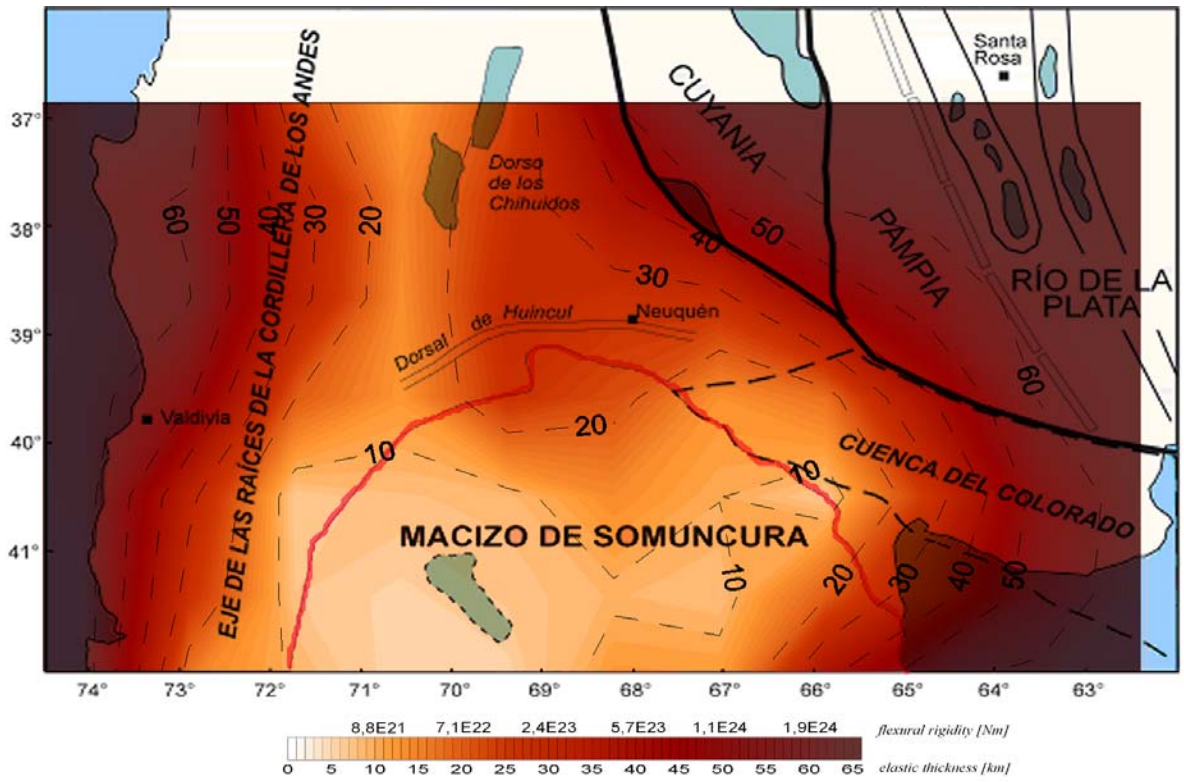

Figure 3.3.6) The elastic thickness isolines calculated for the load model and a reference depth $35km$ was overlain with structural units proposed by RAMOS ET AL. (2002).

The southern part of the Andes is characterized by lower elastic thickness values indicating a softer crust. The Andean orogen in the northern part of the study area is characterized by higher T_e / D values, which indicates a rigid crust. Therefore the area of investigation is separated into a northern and southern segment (WIENECKE 2002).
In the area of the Macizo de Somuncura defined by RAMOS ET AL. (2001) I observe low elastic thickness values of $T_e \leq 15km$ (Fig.3.3.6), computed for the load model with the reference depth of $35km$. This is in very good agreement with the assumption of a mantle upwelling in that area (ROSENAU PERS. COMM.). The structures proposed by RAMOS ET AL. (2001) in the eastern part correlates very well with the T_e / D distribution: The faults of the recent rift system of the passive margin are located in an area of high T_e / D values, predicting a rigid crust. At $71°W$ I obtain a local structure of low T_e / D values striking from N to S.

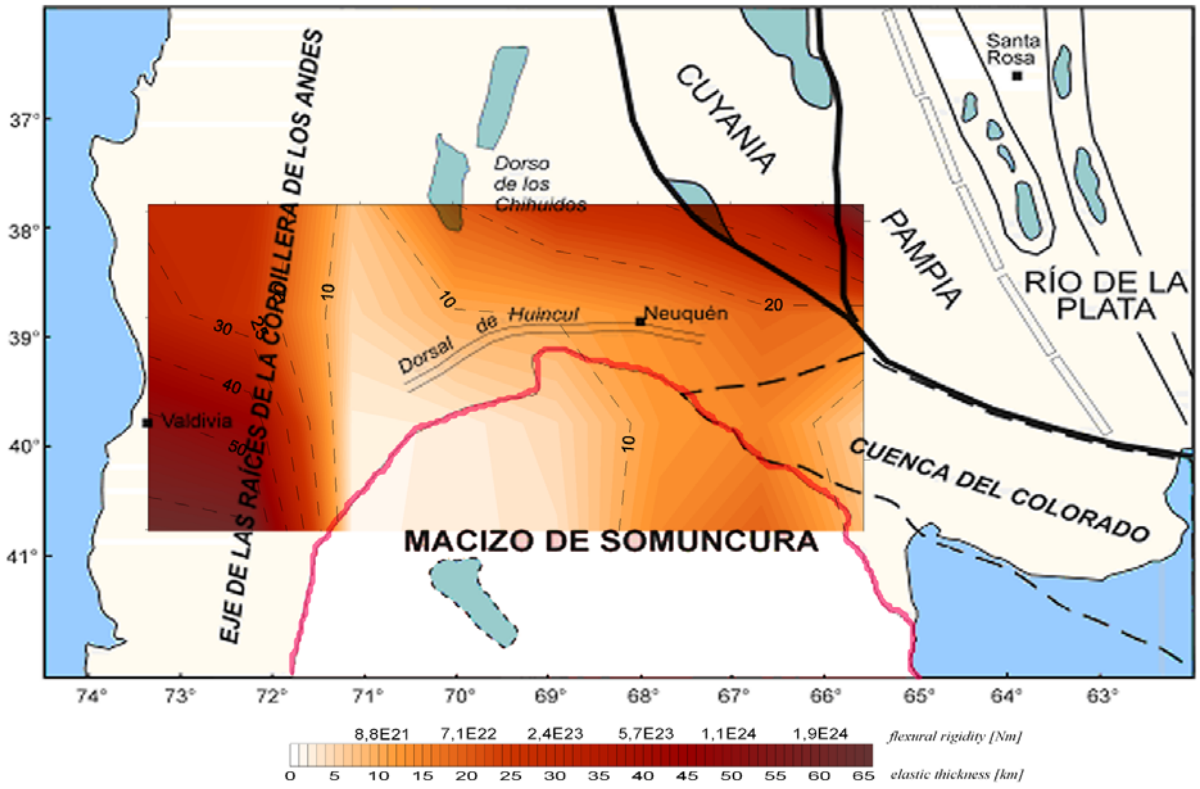

Figure 3.3.7) The elastic thickness distribution obtained for pseudo topography for reference depth $30km$ was overlain with structural units proposed by RAMOS ET AL. (2002).

The results for the pseudo topography show a good correlation between the structures according to RAMOS ET AL. (2002) and the T_e / D variation as well (Fig. 3.3.7). The structure of T_e / D lower values is obtained at $71°W$. In order to investigate this local structure I compare the results with the tectonical units proposed by ROSENAU & ECHTLER (PERS. COMM.) and described by WIENECKE (2002).

The eastern part of the study area is dominated by three structures (Fig. 3.3.8 and 3.3.9): a Precambrian craton (marked with 1a), a failed rift (1b) and a rifted margin (1c). These units are characterized by high elastic thickness/flexural rigidity values of $T_e \geq 30km$ predicting a rigid crust. In the central part of the study area the Neuquen Basin is located (marked in red) which Mesozoic sediment deposits originating from the main cordillera characterize. The location of the main cordillera correlates very well with lower values of $T_e \leq 20km$. The transition zone (marked with 3d) divides the study area in a northern and southern part (ROSENAU PERS. COMM., WIENECKE 2002). The northern part is characterized by higher T_e / D values. The back-arc basins are located in the west of the study area. These basins are indicated by lower T_e / D values. The exhumed accretionary wedge correlates well with higher T_e / D values.

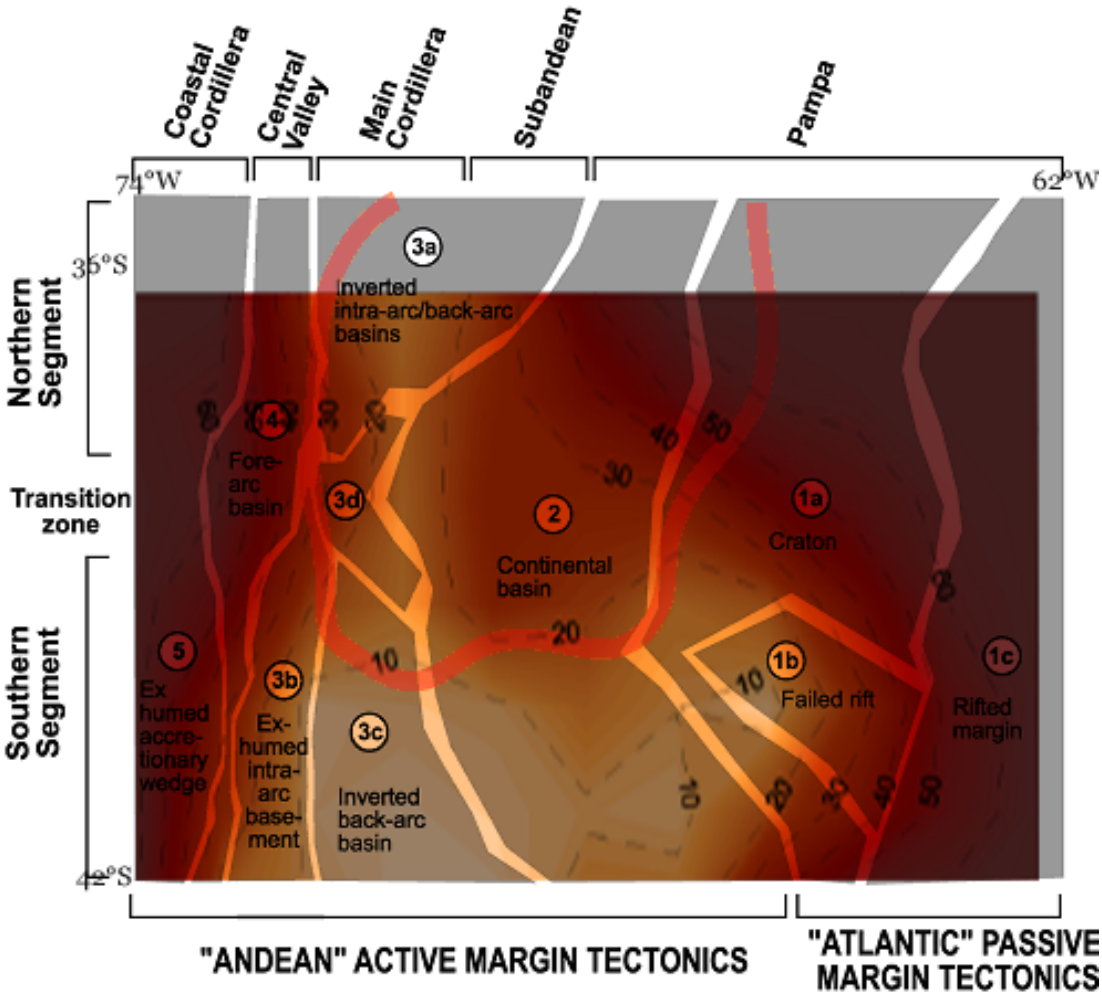

Figure 3.3.8) The elastic thickness/rigidity distribution obtained for load model was overlain with tectonical-structural units according to ECHTLER UND ROSENAU (PERS. COMM.). The Neuquen-Basin is marked in red color (source: WIENECKE 2002).

An equal correlation to the tectonical-structural units is observed for the T_e / D distribution in the pseudo topography model. Thereby the back arc basins are characterized by low T_e / D values as well. I conclude that the study area is divided into a northern and a southern segment, whereby the southern segment is characterized by lower T_e / D values in contrast to the northern part. The different style of topography might result from the difference in rigidity of the crust. However, there are plenty of reasons and driving factors creating a differentiated architecture of the Andean orogen, giving a complete interpretation goes beyond this study. The precision of the calculation is investigated in the following Chapter 4.

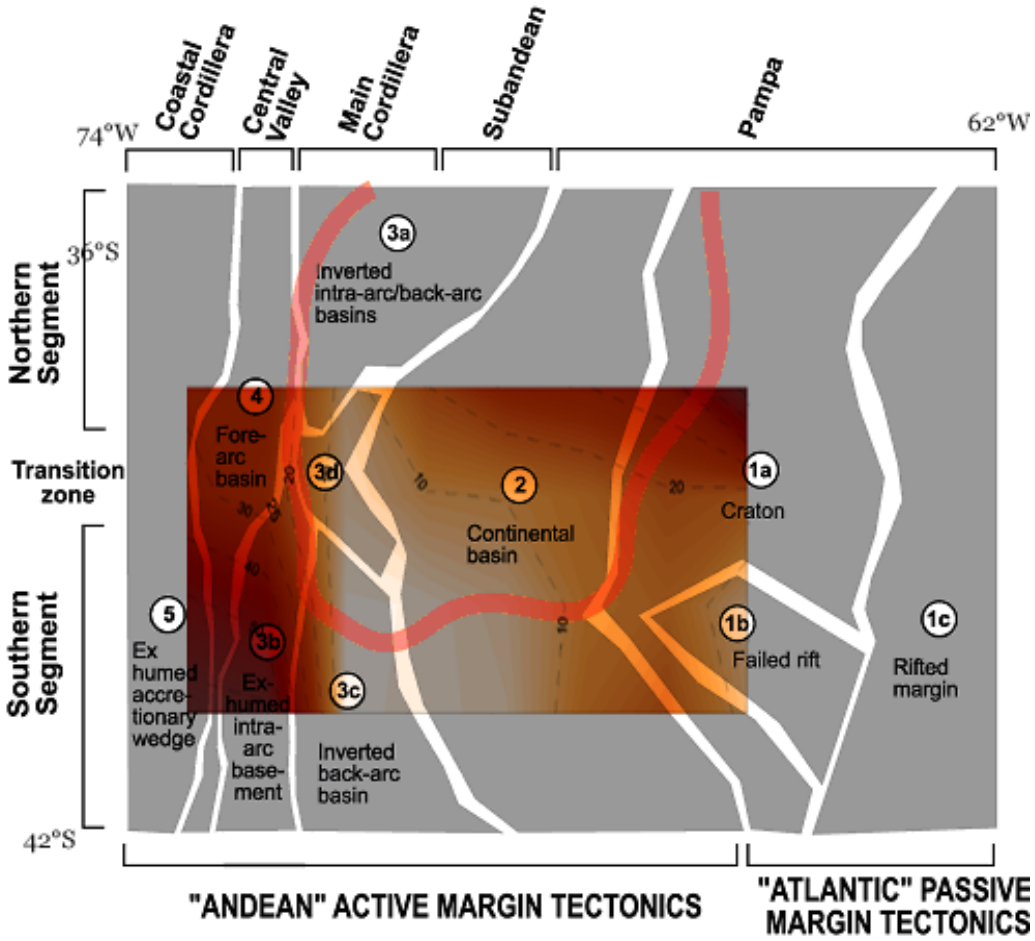

Figure 3.3.9) The elastic thickness/rigidity distribution obtained for pseudo topography was overlain with tectonical-structural units according to ECHTLER UND ROSENAU (PERS. COMM.). The Neuquen-Basin is marked in red color (source: WIENECKE 2002).